Monthly Notices of the ROYAL ASTRONOMICAL SOCIETY

MNRAS **465,** 926–940 (2017) doi:10.1093/mnras/stw2687
Advance Access publication 2016 October 19

# Limits on Population III star formation with the most iron-poor stars

M. de Bennassuti,[1,2★] S. Salvadori,[3,4,5] R. Schneider,[2,5] R. Valiante[2] and K. Omukai[5,6]

[1]*Dipartimento di Fisica, Sapienza, Università di Roma, Piazzale Aldo Moro 5, I-00185 Roma, Italy*
[2]*INAF – Osservatorio Astronomico di Roma, Via di Frascati 33, I-00078 Monte Porzio Catone, Italy*
[3]*Laboratoire d'Etudes des Galaxies, Etoiles, Physique et Instrumentation GEPI, Observatoire de Paris, Place Jules Jannsen, F-92195 Meudon, Paris, France*
[4]*Kapteyn Astronomical Institute, University of Groningen, Landleven 12, NL-9747 AD Groningen, the Netherlands*
[5]*Kavli Institute for Theoretical Physics, Kohn Hall, University of California, Santa Barbara, CA 93106, USA*
[6]*Astronomical Institute, Tohoku University, Aoba, Sendai 980-8578, Japan*

Accepted 2016 October 17. Received 2016 October 17; in original form 2016 June 1

## ABSTRACT

We study the impact of star-forming minihaloes, and the initial mass function (IMF) of Population III (Pop III) stars, on the Galactic halo metallicity distribution function (MDF) and on the properties of C-enhanced and C-normal stars at [Fe/H] $< -3$. For our investigation we use a data-constrained merger tree model for the Milky Way formation, which has been improved to self-consistently describe the physical processes regulating star formation in minihaloes, including the poor sampling of the Pop III IMF. We find that only when star-forming minihaloes are included the low-Fe tail of the MDF is correctly reproduced, showing a plateau that is built up by C-enhanced metal-poor stars imprinted by primordial faint supernovae. The incomplete sampling of the Pop III IMF in inefficiently star-forming minihaloes ($<10^{-3}\,\mathrm{M_\odot\ yr^{-1}}$) strongly limits the formation of pair-instability supernovae (PISNe), with progenitor masses $m_{\mathrm{PopIII}} = [140\text{–}260]\,\mathrm{M_\odot}$, even when a flat Pop III IMF is assumed. Second-generation stars formed in environments polluted at >50 per cent level by PISNe are thus extremely rare, corresponding to ≈0.25 per cent of the total stellar population at [Fe/H] $< -2$, which is consistent with recent observations. The low-Fe tail of the MDF strongly depends on the Pop III IMF shape and mass range. Given the current statistics, we find that a flat Pop III IMF model with $m_{\mathrm{PopIII}} = [10\text{–}300]\,\mathrm{M_\odot}$ is disfavoured by observations. We present testable predictions for Pop III stars extending down to lower masses, with $m_{\mathrm{PopIII}} = [0.1\text{–}300]\,\mathrm{M_\odot}$.

**Key words:** stars: formation – stars: Population II – stars: Population III – supernovae: general – Galaxy: evolution – galaxies: ISM.

## 1 INTRODUCTION

According to the standard Λ cold dark matter (ΛCDM) model for structure formation, the first stars formed at $z \approx 20$ in low-mass dark matter 'minihaloes', with total masses $M \approx [10^6\text{–}10^7]\,\mathrm{M_\odot}$ and virial temperatures $T_{\mathrm{vir}} < 10^4$ K (e.g. Abel, Bryan & Norman 2002; Bromm 2013, for a recent review). At these low temperatures, and in gas of primordial composition, the only available coolant is molecular hydrogen, $H_2$, which can be easily photodissociated by Lyman–Werner (LW) photons ($E = 11.2\text{–}13.6$ eV) produced by the first and subsequent stellar generations (e.g. Haiman, Rees & Loeb 1997; Omukai & Nishi 1999; Machacek, Bryan & Abel 2001). The ability of minihaloes to efficiently form stars is therefore highly debated, and it critically depends upon the specific physical properties of these low-mass systems, such as their formation redshift, gas temperature, and gas metallicity, which determine the cooling efficiency of the gas (e.g. Omukai 2012).

During the epoch of reionization, furthermore, the gas surrounding star-forming galaxies gets ionized and heated up to temperatures $T > 10^4$ K (e.g. Maselli, Ferrara & Ciardi 2003; Graziani et al. 2015). Gas infall is thus suppressed in low-temperature minihaloes born in ionized cosmic regions and it is completely quenched after the end of reionization, at $z \approx 6$ (e.g. Gnedin 2000; Okamoto, Gao & Theuns 2008; Noh & McQuinn 2014; Graziani et al. 2015). Because of the intrinsic fragility of minihaloes, many galaxy formation models neglect star formation in these low-mass systems (e.g. Oñorbe et al. 2015). However, minihaloes likely played an important role in the early Universe, being the nursery of the first stars and the dominant halo population, which likely regulated the initial phases of reionization and chemical enrichment (e.g. Salvadori et al. 2014; Wise et al. 2014).

★ E-mail: matteo.debennassuti@oa-roma.inaf.it

During last years, observational evidences of the importance of minihaloes have been provided by ultrafaint dwarf galaxies, the faintest and most metal-poor galaxy population in the Local Group (Simon & Geha 2007). These galaxies, which have total luminosities $L < 10^5\,L_\odot$, have been proposed to be the living fossil of the minihaloes which overcame radiative feedback processes and managed to form stars before the end of reionization (Bovill & Ricotti 2009; Muñoz et al. 2009; Salvadori & Ferrara 2009). Deep colour–magnitude diagrams of ultrafaint dwarfs have confirmed these theoretical predictions, showing that these small systems are typically dominated by >13-Gyr old stars, which therefore formed at $z > 6$. In addition, many carbon-enhanced metal-poor (CEMP) stars have been found in ultrafaint dwarf galaxies (Norris et al. 2010; Simon et al. 2010; Frebel et al. 2015), with respect to the more massive and more luminous 'classical' dwarf spheroidal galaxies (Skúladóttir et al. 2015). The high incidence of these peculiar stars, which have [C/Fe] > 0.7 and were likely imprinted by the very first stars (de Bennassuti et al. 2014), is an additional confirmation that ultrafaint galaxies are likely the living relics of star-forming minihaloes from the pre-reionization epoch (Salvadori, Skúladóttir & Tolstoy 2015).

Accounting for the star formation in minihaloes is thus an essential step to study the early phases of galaxy evolution and the impact on current stellar sample of 'second-generation' stars, which formed out of gas polluted by the first stars. In a previous paper, we studied the implication of the properties of the most iron-poor stars observed in the Galactic halo for the initial mass function (IMF) of the first Population III (Pop III) stars (de Bennassuti et al. 2014). To this aim, we use the cosmological merger-tree code GAmete MErger Tree and Evolution (GAMETE; Salvadori, Schneider & Ferrara 2007; Salvadori, Ferrara & Schneider 2008) which was implemented to self-consistently account for the production and destruction of dust, and for a two-phase interstellar medium (Valiante et al. 2011; de Bennassuti et al. 2014). However, we did not account for star formation in minihaloes, as instead it was done in many other applications and further implementations of the model (e.g. Salvadori & Ferrara 2009, 2012; Salvadori, Dayal & Ferrara 2010; Ferrara et al. 2014; Salvadori et al. 2014, 2015; Valiante et al. 2016).

In de Bennassuti et al. (2014), we showed that dust cooling is required to explain the existence of the most pristine, carbon-normal star at $Z \approx 10^{-4.5}\,Z_\odot$ (Caffau et al. 2011). This implies that the transition from massive Pop III stars, to normal, Population II (Pop II) stars, is (also) driven by thermal emission of collisionally excited dust and thus can occur at a critical dust-to-gas mass ratio $\mathcal{D}_{\rm cr} > 4.4 \times 10^{-9}$ (Schneider et al. 2002, 2006, 2012b). Furthermore, we showed that CEMP-no stars (which show no r-/s- process elements, see Section 3) are likely imprinted by the so-called 'primordial faint supernovae' (SNe), i.e. Pop III stars with typical progenitor masses of $m_{\rm PopIII} = [10\text{–}40]\,M_\odot$ that during their evolution experience mixing and fallback and eject small amounts of $Ni^{56}$, producing a faint light curve (Bonifacio, Limongi & Chieffi 2003). Our results pointed out that these pristine and relatively massive stars should dominate the early metal enrichment to successfully reproduce the observed fraction of carbon-enhanced versus carbon-normal stars. In particular, we put constraints on the Pop III IMF, which should be limited to the mass range $m_{\rm PopIII} = [10\text{–}140]\,M_\odot$. Note that state-of-the-art numerical simulations of the first cosmic sources performed by different groups predict disparate Pop III star masses (e.g. Greif 2015, for a recent review), with plausible mass ranges that can vary from subsolar values (e.g. Stacy, Bromm & Lee 2016) up to $m_{\rm PopIII} \approx 1000\,M_\odot$ (e.g. Hirano et al. 2014, 2015; Susa, Hasegawa & Tominaga 2014; Hosokawa et al. 2016).

In this paper, we investigate the impact of the Pop III IMF on the properties of CEMP and C-normal stars by accounting for star-forming minihaloes. To this aim, we further develop the model to catch the essential physics required to self-consistently trace the formation of stars in minihaloes by including:

(i) a star formation efficiency that depends on the gas temperature, gas metallicity, and formation redshift of minihaloes, and on the average value of the LW background;
(ii) a random sampling treatment of the IMF of Pop III stars, which inefficiently form in minihaloes;
(iii) a suppression of gas infall in minihaloes born in ionized regions, using a self-consistent calculation of reionization.

The paper is organized as follows. In Section 2 we summarize the main features of our cosmological model, mainly focusing on the new physics implemented here. In Section 3, we briefly recap available observations of very metal-poor stars in the Galactic halo, including the new findings. Model results are presented in Section 4, where we show the effects of different physical processes on the Galactic halo metallicity distribution function (MDF) and on the fraction of carbon-enhanced versus carbon-normal stars. Finally, in Section 5, we critically discuss the results and provide our conclusions.

## 2 DESCRIPTION OF THE MODEL

In this section we briefly summarize the main features of the semi-analytical code GAMETE and describe in full detail the model implementations that we made for the purpose of this work.

GAMETE is a cosmological merger tree model in the ΛCDM framework[1] that traces the star formation history and chemical evolution of Milky Way (MW)-like galaxies from redshift $z = 20$ down to the present-day. The code reconstructs a statistical significant sample of independent merger histories of the MW dark matter halo by using a binary Monte Carlo code, which is based on the extended Press–Schechter (EPS) theory (e.g. Bond et al. 1991) and accounts for both halo mergers and mass accretion (Salvadori et al. 2007). As shown by Parkinson, Cole & Helly (2008), merger trees obtained through the EPS formalism are in good agreement with the halo merger histories of *N*-body simulations (e.g. the Millennium Simulation; Springel et al. 2005) and the same is true for the specific case of the MW Galaxy (e.g. Salvadori 2009, fig. 2.3). Since semi-analytical models can rapidly run on merger trees, this approach enables us to efficiently explore the effects of different model parameters on a large sample of possible assembly histories of our Galaxy, which is unknown. Hence, it is the perfect statistical tool to study the impact of the Pop III IMF on the observed properties of present-day stars while accounting for the uncertainties induced by different assembling histories. To reconstruct the possible MW merger histories, we assume that the Galaxy is embedded in a dark matter (DM) halo of mass $M_{\rm MW} = 10^{12}\,M_\odot$ at $z = 0$, which is in agreement with current measurements and uncertainties: $1.26^{+0.24}_{-0.24} \times 10^{12}\,M_\odot$ (McMillan 2011), $0.9^{+0.4}_{-0.3} \times 10^{12}\,M_\odot$ (Kafle et al. 2012), $0.80^{+0.31}_{-0.16} \times 10^{12}\,M_\odot$ (Kafle et al. 2014, see also Wang et al. 2015 for the different methods adopted to infer the DM mass). The 50 possible MW merger histories we reconstruct resolve minihaloes down to a virial temperature $T_{\rm vir} = 2 \times 10^3$ K (e.g. see de Bennassuti et al. 2014). We use 50 possible MW merger histories

[1] We assume a *Planck* cosmology with $h_0 = 0.67$, $\Omega_{\rm b}\,h^2 = 0.022$, $\Omega_{\rm m} = 0.32$, $\Omega_\Lambda = 0.68$, $\sigma_8 = 0.83$, $n_{\rm s} = 0.96$ (Planck Collaboration XVI 2014).

because we find that the results converge with this number of realizations, thus a larger number would not provide any improvement in our findings.

The star formation and chemical evolution history of the MW is then traced along the merger trees. We assume that the gas inside dark matter haloes can be converted into stars at a rate $\psi(t) = \epsilon_* M_{\rm ISM}(t)/t_{\rm dyn}(t)$, where $\epsilon_*$ is the star formation efficiency, $t_{\rm dyn}(t)$ the dynamical time-scale, and $M_{\rm ISM}(t)$ the total mass of gas into the interstellar medium (ISM), which is regulated by star formation, SN-driven outflows, and by a numerically calibrated infall rate (Salvadori et al. 2008). Because of less efficient gas cooling, the star formation efficiency in minihaloes ($T_{\rm vir} < 10^4$ K), $\epsilon_{\rm MH}$, is smaller than that of Ly$\alpha$-cooling haloes ($T_{\rm vir} \geq 10^4$ K), $\epsilon_*$ (see Section 2.1).

Once stars are formed, we follow their subsequent evolution using mass- and metallicity-dependent lifetimes (Raiteri, Villata & Navarro 1996), metal (Woosley & Weaver 1995; van den Hoek & Groenewegen 1997; Heger & Woosley 2002) and dust (Schneider, Ferrara & Salvaterra 2004; Bianchi & Schneider 2007; Marassi et al. 2014, 2015) yields. Chemical evolution is followed in all star-forming haloes and in the surrounding MW environment enriched by SN-driven outflows regulated by a wind efficiency $\epsilon_{\rm w}$, which represents the fraction of SN explosion energy converted into kinetic form (Salvadori et al. 2008). While $\epsilon_{\rm w}$ is assumed to be the same for all dark matter haloes, the ejected mass is evaluated by comparing the SN kinetic energy with the halo binding energy. Following equation (9) of Salvadori et al. (2008), we thus have

$$\frac{{\rm d}M_{\rm ej}}{{\rm d}t} \propto \frac{\epsilon_{\rm w}}{v_{\rm circ}^2}, \tag{1}$$

where $v_{\rm circ}$ is the halo circular velocity.

As discussed in de Bennassuti et al. (2014), the evolution of the ISM in each progenitor halo is described as follows.

(i) We assume the ISM to be characterized by two phases. (a) A cold, *dense* phase that mimics the properties of molecular clouds (MCs). In this dense phase star formation occurs and dust grains accrete gas-phase metals. (b) A hot, *diffuse* phase that exchanges mass with the MW environment through gas infall and SN winds. In this diffuse phase, SN reverse shocks can partially destroy newly produced dust grains (Bianchi & Schneider 2007; Marassi et al. 2015; Bocchio et al. 2016).

(ii) Chemical evolution is described separately in the two phases, but the mass exchange between the dense and diffuse ISM is taken into account, through the condensation of the diffuse phase and the dispersion of MCs which return material to the diffuse phase. These processes are regulated by two additional free parameters, as described in section 2.1 of de Bennassuti et al. (2014).

(iii) The transition from massive, Pop III stars to 'normal' Pop II stars is assumed to be driven by dust grains (e.g. Schneider et al. 2002) and to occur when the dust-to-gas mass ratio in the dense phase exceeds the critical value $\mathcal{D}_{\rm cr} = 4.4 \times 10^{-9}$ (Schneider et al. 2012a).

(iv) Pop III stars form with masses in the range [10–300] $\rm M_\odot$ according to a Larson-type IMF:

$$\Phi(m) = \frac{{\rm d}N}{{\rm d}m} \propto m^{\alpha-1} \exp\left(-\frac{m_{\rm ch}}{m}\right), \tag{2}$$

with $m_{\rm ch} = 20\,\rm M_\odot$ and $\alpha = -1.35$ (de Bennassuti et al. 2014). We assume that chemical enrichment (metals and dust) is driven by Pop III stars with masses [10–40] $\rm M_\odot$, which explode as faint SNe, and by stars with masses [140–260] $\rm M_\odot$, which explode as pair-instability supernovae (PISNe; e.g. Heger & Woosley 2002; Schneider et al. 2004; Takahashi et al. 2016). We recall that these 'faint SNe' experience mixing and fallback during their evolution (Bonifacio et al. 2003). As a consequence, when they explode as SNe, they eject small amounts of $\rm Ni^{56}$ (and hence Fe) with respect to other light elements, such as C (e.g. Umeda & Nomoto 2003; Iwamoto et al. 2005; Tominaga, Umeda & Nomoto 2007; Ishigaki et al. 2014; Marassi et al. 2014). The Fe and C yields adopted in this work (Marassi et al. 2014, 2015) are in agreement with the findings of other groups that assumed similar faint SN models (e.g. Iwamoto et al. 2005; Tominaga et al. 2007; Ishigaki et al. 2014). Note that other scenarios have been proposed for the evolution of Pop III stars in this relatively low mass range, such as the rapidly rotating 'spinstars' (e.g. Meynet, Ekström & Maeder 2006; Maeder, Meynet & Chiappini 2015). Still, even in these cases, the yields of Fe and C are very similar to those produced by the faint SNe adopted in this work.

(v) Pop II stars form according to a Larson IMF with $m_{\rm ch} = 0.35\,\rm M_\odot$, $\alpha = 1.35$, and masses in the range [0.1–100] $\rm M_\odot$. Their contribution to chemical enrichment is driven by asymptotic giant branch (AGB) stars ($2 \leq m_{\rm PopII} \leq 8\,\rm M_\odot$) and by ordinary core-collapse SNe ($8 < m_{\rm PopII} \leq 40\,\rm M_\odot$).

We refer the reader to the aforementioned papers for a detailed description of the basic features of the model. In the next subsections we illustrate how we implemented star formation in $H_2$ cooling minihaloes.

### 2.1 Gas cooling in minihaloes

The gas cooling process in minihaloes relies on the presence of molecular hydrogen, $H_2$, which can be easily photodissociated by photons in the LW band. Several authors have shown that ineffective cooling by $H_2$ molecules limits the amount of gas that can be converted into stars, with efficiencies that decrease proportional to $T_{\rm vir}^3$ (e.g. Madau, Ferrara & Rees 2001; Okamoto et al. 2008). For this reason, models that account for minihaloes, typically assume that in these small systems the star formation efficiency is reduced with respect to more massive Lyman $\alpha$ cooling haloes, and that the ratio between the two efficiencies is a function of the virial temperature, $\epsilon_{\rm MH}/\epsilon_* = 2[1 + (T_{\rm vir}/2 \times 10^4\,{\rm K})^{-3}]^{-1}$ (e.g. Salvadori & Ferrara 2009, 2012). This simple relation is illustrated in the right-hand panels of Fig. 1 (dashed lines).

However, the ability of minihaloes to cool down their gas not only depends on $T_{\rm vir}$, but also on their formation redshift, on the gas metallicity, and on the LW flux, $J_{\rm LW}$, to which these systems are exposed. In this work, we compute the mass fraction of gas that is able to cool in one dynamical time following a simplified version of the chemical evolution model of Omukai (2012). For a more detailed description of the model and of the gas-cooling processes that we have considered, we refer the reader to the appendix A of Valiante et al. (2016).[2]

In Fig. 1 we show the resulting efficiencies, $\epsilon_{\rm MH}$, normalized to $\epsilon_*$ for different gas metallicities (left), minihalo virial temperatures (right), and LW flux. The different lines show different mini-halo formation redshifts. When the LW background is neglected, i.e. $J_{21} = J_{\rm LW}/(10^{-21}\,{\rm erg\,cm^{-2}/s^{-1}\,Hz^{-1}\,sr^{-1}}) = 0$ (upper panels), we can clearly see the dependence of $\epsilon_{\rm MH}/\epsilon_*$ on (i) the formation redshift, (ii) the gas metallicity (left), and (iii) the virial temperature

[2] Here we correct the derivation of the cooling time (equation A2 in Valiante et al. 2016) by dividing equation (19) of Madau et al. (2001) for $\Omega_{\rm m}$. This enhances the star formation efficiencies shown in their figs A1–A4 (see Fig. 1).

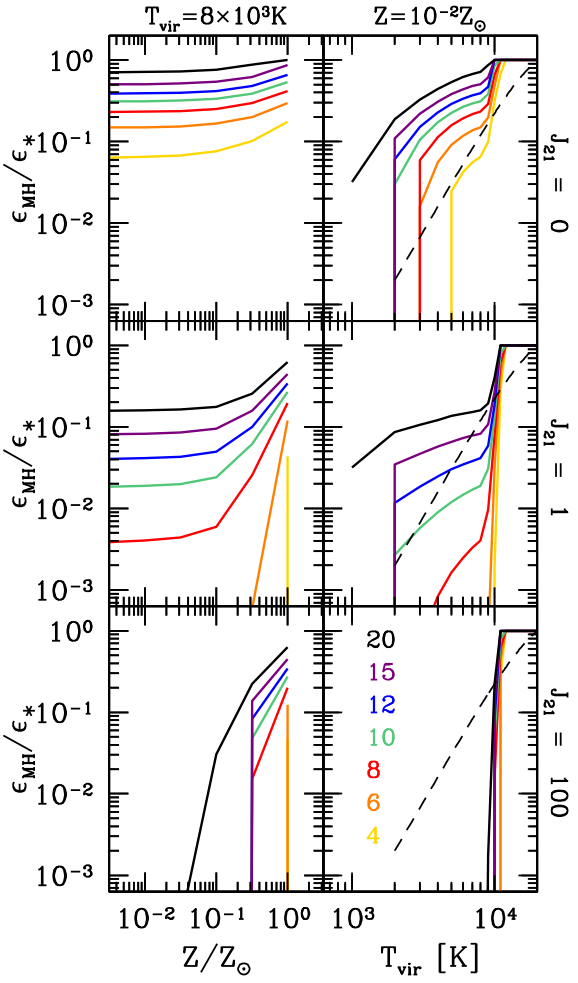


**Figure 1.** The ratio between the star formation efficiency in minihaloes, $\epsilon_{\rm MH}$, and the constant efficiency of Lyman $\alpha$ cooling haloes $\epsilon_*$ (see text). The coloured lines represent different minihaloes formation redshifts ($z$ = 20, 15, 12, 10, 8, 6, 4, from top to bottom, as explained in the legends). Upper, middle, and lower panels show the results assuming $J_{21} = J_{\rm LW}/(10^{-21}\,{\rm erg\,cm^{-2}\,s^{-1}\,Hz^{-1}\,sr^{-1}}) = 0$, 1, and 100, respectively. Left-hand panels: dependence on the gas metallicity for a fixed $T_{\rm vir} = 8 \times 10^3$ K; at $Z < 10^{-2.5}\,{\rm Z}_\odot$ the ratio $\epsilon_{\rm MH}/\epsilon_*$ is constant. Right-hand panels: dependence on the virial temperature, for a fixed $Z = 10^{-2}\,{\rm Z}_\odot$. The dashed lines show the $z$-independent relation used in Salvadori & Ferrara (2009, 2012).

(right). As a general trend, we find that the smaller are these quantities, the lower is the gas-cooling efficiency of minihaloes. At $T_{\rm vir} \geq 10^4$ K, Lyman $\alpha$ cooling becomes efficient and $\epsilon_{\rm MH}/\epsilon_* = 1$. When $J_{21} \sim 1$ (middle panels), gas cooling is partially suppressed due to $H_2$ photodissociation. When $z > 8$, the gas is dense enough to self-shield against the external LW background, and $\epsilon_{\rm MH}$ decreases only by 1 dex with respect to the $J_{21} = 0$ case. When $z \leq 8$, gas cooling is completely suppressed in $T_{\rm vir} < 10^4$ K systems, unless they are already enriched to $Z \sim {\rm Z}_\odot$. This is consistent with the minimum halo mass to form stars assumed in Salvadori & Ferrara (2009, 2012). Similarly, when minihaloes are exposed to a stronger LW flux, $J_{21} \sim 100$ (lower panels), gas cooling is allowed only at $z > 8$ in highly enriched minihaloes, which have $Z \gtrsim 10^{-1.5}\,{\rm Z}_\odot$. In what follows, we will use the results in Fig. 1 to self-consistently compute the star-formation efficiency of minihaloes in our merger trees.

### 2.2 Stochastic Pop III IMF

The mass of newly formed stars in a given dark matter halo depends on the gas mass and star formation efficiency. In low-mass systems the available mass of gas can be strongly reduced with respect to the initial mean cosmic value, $\Omega_{\rm b}/\Omega_{\rm M}$, because of SN-driven outflows and radiative feedback processes (e.g. Salvadori & Ferrara 2009). Furthermore, due to the reduced cooling efficiency minihaloes (see Fig. 1), the total stellar mass formed in each burst is small, $M^{\rm tot}_{\rm PopIII} < 10^4\,{\rm M}_\odot$. In these conditions, the resulting stellar mass spectrum will be affected by the incomplete sampling of the underlying stellar IMF. This effect can be particularly relevant for Pop III stars, which have masses in the range [10–300] $\rm M_\odot$ (e.g. Hirano et al. 2014). Hence, we adopt a random-selection procedure, the result of which is illustrated in Fig. 2.

The stars produced during each burst of star formation are randomly selected within the IMF mass range, and they are assumed to form with a probability that is given by the IMF normalized to the total mass of stars formed in each burst. In Fig. 2 we show the comparison between the randomly selected and the intrinsic IMF for total stellar masses of $M^{\rm tot}_{\rm PopIII} = (10^2, 10^3, 10^4, 10^6)\,{\rm M}_\odot$. When $M^{\rm tot}_{\rm PopIII} \gtrsim 10^5\,{\rm M}_\odot$ the overall mass range can be fully sampled and the intrinsic IMF is well reproduced. On the other hand, the lower is the stellar mass formed, the worse is the match between the sampled and the intrinsic IMF. In particular, when $M^{\rm tot}_{\rm PopIII} \leq 10^3\,{\rm M}_\odot$, it becomes hard to form Pop III stars with $m_{\rm PopIII} = [140–260]\,{\rm M}_\odot$ (PISN progenitor mass range). We find that while almost 100 per cent of the haloes forming $10^4\,{\rm M}_\odot$ Pop III stars host ≈9 PISNe each, only 60 per cent of the haloes producing $10^3\,{\rm M}_\odot$ of Pop III stars host *at most* 1 PISN. Thus, we find that the number of PISN is naturally limited by the incomplete sampling of the stellar IMF.

### 2.3 Radiative feedback

To self-consistently account for the effect of radiative feedback processes acting on minihaloes, we compute the amount of radiation in the LW (11.2–13.6 eV) and ionizing (>13.6 eV) bands produced by star-forming haloes along the merger trees. We take time- and metallicity-dependent UV luminosities from Bruzual & Charlot (2003) for Pop II stars and from Schaerer (2002) for Pop III stars.[3]

Input values used for Pop II stars of different stellar metallicities are shown in Fig. 3 as a function of stellar ages. As expected, the UV luminosity is largely dominated by young stars and depends on stellar metallicity, as more metal-poor stars have harder emission spectra. In the first 10 Myr, the ionizing photon rate drops from $>2 \times 10^{46}$ to $<2 \times 10^{45}$ photons/s/$\rm M_\odot$, while the rate of LW photons remains approximately constant at $\sim 10^{46}$ photons/s/$\rm M_\odot$. Therefore, although initially lower, after 10 Myr the rate of LW photons emitted becomes higher than that of ionizing photons.

In the following, we describe how we compute the LW and ionizing background and how we account for reionization of the MW environment. Given the lack of spatial information, we assume that the time-dependent LW and ionizing radiation produced by stars build-up a homogeneous background, which – at each given redshift – affects all the (mini-)haloes in the same way.

[3] We use the photon luminosities from table 4 of Schaerer (2002) for metal-free stars.

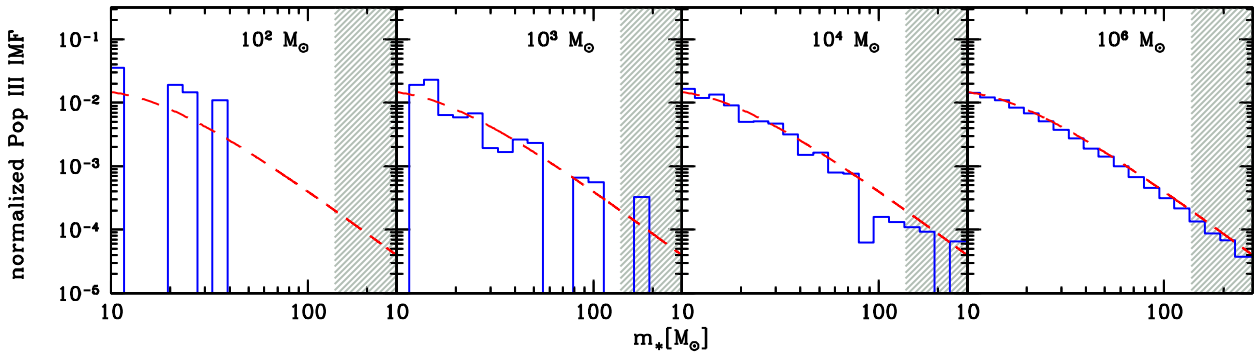


**Figure 2.** Comparison between the intrinsic IMF of Pop III stars (red dashed lines) and the effective mass distribution resulting from the random sampling procedure (blue histograms). In each panel, the IMF is normalized to the total stellar mass formed, with $M^{\rm tot}_{\rm PopIII} = (10^2, 10^3, 10^4, 10^6)\,{\rm M}_\odot$ (from left to right). The grey shaded areas indicate the progenitor mass range of PISNe (see text).

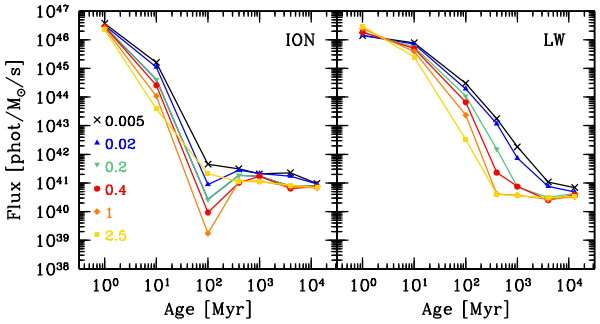


**Figure 3.** Ionizing (left) and LW (right) photon luminosities per unit stellar mass of Pop II stars as a function of stellar age (Bruzual & Charlot 2003). Different colours refer to different metallicities as shown by the labels: $Z/{\rm Z}_\odot = 0.005$, 0.02, 0.2, 0.4, 1, 2.5 (black crosses, blue up-triangles, green down-triangles, red dots, orange diamonds, gold squares).

### 2.3.1 *LW background*

The cumulative flux observed at a given frequency $\nu_{\rm obs}$ and redshift $z_{\rm obs}$ can be computed by accounting for all stellar populations that are still evolving at $z_{\rm obs}$ (Haardt & Madau 1996):

$$J(\nu_{\rm obs}, z_{\rm obs}) = (1+z_{\rm obs})^3 \frac{c}{4\pi} \int_{z_{\rm obs}}^{\infty} {\rm d}z \left|\frac{{\rm d}t}{{\rm d}z}\right| \epsilon(\nu', z)\, {\rm e}^{-\tau(\nu_{\rm obs}, z_{\rm obs}, z)}, \quad (3)$$

where

$$\left|\frac{{\rm d}t}{{\rm d}z}\right| = \{H_0(1+z)[\Omega_{\rm m}(1+z)^3 + \Omega_\Lambda]^{1/2}\}^{-1}, \quad (4)$$

$\nu' = \nu_{\rm obs}(1+z)/(1+z_{\rm obs})$, $\epsilon(\nu', z)$ is the comoving emissivity at frequency $\nu'$ and redshift $z$, and $\tau(\nu_{\rm obs}, z_{\rm obs}, z)$ is the MW environment optical depth affecting photons emitted at redshift $z$ and seen at redshift $z_{\rm obs}$ at frequency $\nu_{\rm obs}$ (Ricotti, Gnedin & Shull 2001).

To obtain the average flux in the LW band, we integrate equation (3) between $\nu_{\rm min} = 2.5 \times 10^{15}$ Hz (11.2 eV) and $\nu_{\rm max} = 3.3 \times 10^{15}$ Hz (13.6 eV):

$$J_{\rm LW}(z_{\rm obs}) = \frac{1}{\nu_{\rm max} - \nu_{\rm min}} \int_{\nu_{\rm min}}^{\nu_{\rm max}} {\rm d}\nu_{\rm obs}\; J(\nu_{\rm obs}, z_{\rm obs}). \quad (5)$$

Following Ahn et al. (2009), we write the mean attenuation in the LW band as

$${\rm e}^{-\tau(z_{\rm obs}, z)} = \frac{\int_{\nu_{\rm min}}^{\nu_{\rm max}} {\rm e}^{-\tau(\nu_{\rm obs}, z_{\rm obs}, z)}\, {\rm d}\nu_{\rm obs}}{\int_{\nu_{\rm min}}^{\nu_{\rm max}} {\rm d}\nu_{\rm obs}}, \quad (6)$$

so that

$$J_{\rm LW}(z_{\rm obs}) = (1+z_{\rm obs})^3 \frac{c}{4\pi} \int_{z_{\rm obs}}^{z_{\rm screen}} {\rm d}z \left|\frac{{\rm d}t}{{\rm d}z}\right| \epsilon_{\rm LW}(z)\, {\rm e}^{-\tau(z_{\rm obs}, z)}, \quad (7)$$

where $\epsilon_{\rm LW}(z)$ is the emissivity in the LW band. Equation (7) is integrated up to $z_{\rm screen}$, that is the redshift above which photons emitted in the LW band are redshifted out of the band (the so-called 'dark screen' effect).

In the top panel of Fig. 4, we show the redshift evolution of the LW background predicted by the fiducial model (see Sections 2.4 and 4). We find that at $z \sim 18$ the average LW background is already $J_{21} \approx 10$, thus strongly reducing the star formation in $T_{\rm vir} < 10^4$ K minihaloes. The point shown at $z = 0$ is the average LW background in the Galactic ISM, and it has been computed from equation (2) of Sternberg et al. (2014). The value refers to a LW central wavelength of 1000 Å, while the error bar represents the variation interval of $J_{21}$ corresponding to all wavelengths in the LW band (i.e. from 912 to 1108 Å). Although the $J_{21}$ background we have obtained is consistent with this data, at high-$z$ our calculations likely overestimate $J_{21}$. In fact, at any given redshift all LW photons are assumed to escape from star-forming galaxies but they are retained into the MW environment. Yet, the mean free path of LW photons (≈10 Mpc; e.g. Haiman et al. 1997) is larger than the physical radius of the Milky Way. In particular, we assume that the MW and its progenitor haloes evolve in a comoving volume ≈5 Mpc$^3$, which we estimate at the turn-around radius (see Salvadori et al. 2014). Hence our code simulates a biased region of the Universe, the high density fluctuation giving rise to the MW and its progenitors. For this reason, the LW flux we obtain is consistent with that found by Crosby et al. (2013) who consider a similar volume. On the other hand, the predicted $J_{21}$ is larger than those obtained by cosmological simulations of the Universe, which account for larger volumes (e.g. Ahn et al. 2009; O'Shea et al. 2015; Xu et al. 2016). However, as we will show in Section 4, such a strong difference in the LW background have a very small impact on our results.

### 2.3.2 *Reionization*

Photons with energies >13.6 eV are responsible for hydrogen (re)ionization. At any given redshift, we compute the ionizing photon rate density, $\dot{n}_{\rm ion}(z)$, by summing the ionizing luminosities over all active stellar populations and dividing by the MW volume, ≈5 Mpc$^3$. The filling factor $Q_{\rm H\,II}$, i.e. the fraction of MW

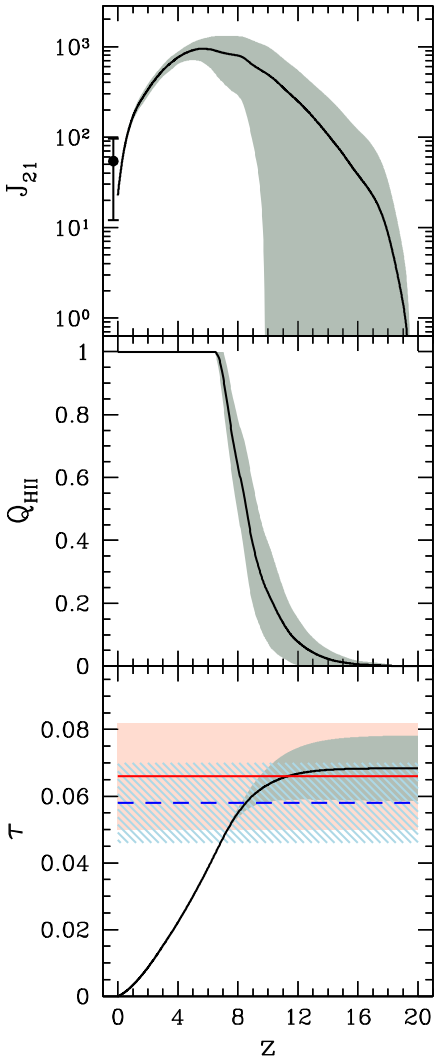


**Figure 4.** Redshift evolution of the LW flux (upper panel), the volume filling factor of ionized regions (middle panel), and the corresponding Thomson scattering optical depth (lower panel) predicted by the fiducial model and obtained by averaging over 50 MW merger histories (solid lines). The shaded areas show the $1\sigma$ dispersion among different realizations. The point with error bar at $z = 0$ represents an estimate of the specific intensity of the isotropic UV radiation field in the Galactic ISM (Sternberg et al. 2014). The red-solid horizontal line shows the *Planck* measurement (Planck Collaboration XIII 2016) with $1\sigma$ dispersion (horizontal filled shaded area). The more recent measurement (Planck Collaboration XLVII 2016) is plotted as a blue-dashed horizontal line with $1\sigma$ dispersion (horizontal striped-dashed shaded area).

volume which has been reionized at a given observed redshift $z_{\rm obs}$, is computed following Barkana & Loeb (2001):

$$Q_{\rm HII}(z_{\rm obs}) = \frac{f_{\rm esc}}{n_{\rm H}^0} \int_{z_{\rm obs}}^{z_{\rm em}} {\rm d}z \left|\frac{{\rm d}t}{{\rm d}z}\right| \dot{n}_{\rm ion}\, {\rm e}^{F(z_{\rm obs},z)}, \quad (8)$$

with

$$F(z_{\rm obs}, z) = -\alpha_{\rm B}\, n_{\rm H}^0 \int_{z_{\rm obs}}^{z} {\rm d}z' \left|\frac{{\rm d}t}{{\rm d}z'}\right| C(z')\,(1+z')^3, \quad (9)$$

where $f_{\rm esc}$ is the escape fraction of ionizing photons, $F(z_{\rm obs}, z)$ accounts for recombinations of ionized hydrogen, and $n_{\rm H}^0$ is the present-day hydrogen number density in the MW environment, which is ≈5 times larger than in the IGM. In equation (9), $\alpha_{\rm B}$ is the case B recombination coefficient,[4] and $C(z)$ is the redshift-dependent clumping factor, which is assumed to be equal to $C(z) = 17.6\,{\rm e}^{(-0.10\,z+0.0011\,z^2)}$ (Iliev, Scannapieco & Shapiro 2005).

Following Salvadori et al. (2014), we assume an escape fraction for ionizing photons $f_{\rm esc} = 0.1$, which provides a reionization history that is complete by $z \sim 6.5$, fully consistent with recent data. This is illustrated in the lower panels of Fig. 4, where we show the redshift evolution of the volume filling factor of ionized regions and the corresponding Thomson scattering optical depth. In addition, Salvadori et al. (2014) show that the same reionization history appears consistent with the star formation histories of dwarf satellites of the MW.

### 2.4 Model calibration

The free parameters of the model are assumed to be the same for all dark matter haloes of the merger trees and they are calibrated by comparing the 'global properties' of the MW as observed today with the average mean value over 50 independent merger histories. In particular, we match the observed mass of stars, metals, dust, and gas, along with the star formation rate (see table 1 of de Bennassuti et al. 2014). All these observed properties are simultaneously reproduced by assuming the same model free parameters of de Bennassuti et al. (2014), table 2. By looking at the predicted evolution of such global properties we can see that at $z = 0$ the $1\sigma$ dispersion among different merger histories becomes smaller than the observational errors (fig. 4 in de Bennassuti et al. 2014). This implies that the global properties are well reproduced not only by the average mean values, but also by each single merger history.

## 3 OBSERVATIONS: VERY METAL-POOR STARS

During the last decades, surveys looking for very metal-poor stars, with [Fe/H] $< -2$, have explored the stellar halo of our Galaxy. One of the main outcomes of these surveys has been the determination of the MDF, namely the number of stars as a function of their iron abundance, [Fe/H], which is used as a metallicity tracer. Early determinations of the MDF by Ryan & Norris (1991) have shown that the MDF peaks around [Fe/H] $= -1.6$, with wings from solar abundances down to [Fe/H] $\approx -3$, although one star at [Fe/H] $\approx -4$ was already discovered thanks to serendipitous detection (Bessell & Norris 1984). Spectroscopic follow-up of the HK survey (Beers, Preston & Shectman 1985) by Molaro & Castelli (1990), Molaro & Bonifacio (1990), and Primas, Molaro & Castelli (1994) showed that the tail extended down to [Fe/H] $\approx -4.0$, and led to the determination of the first carbon-enhanced metal-poor stars (Norris, Ryan & Beers 1997; Bonifacio et al. 1998). More recent observations by the HK and the Hamburg/ESO Survey (HES; e.g. Christlieb et al. 2008) have confirmed the presence of the MDF peak at [Fe/H] $\approx -1.6$ and they have lead to the identification of some hundreds of new stars at [Fe/H] $< -3$ (see Fig. 5). These 'extremely metal-poor stars' are of key importance to understand the early chemical enrichment processes. In particular, it has been shown that the shape of the low-Fe tail of the Galactic halo MDF can shed new light on the properties of the first stellar generations, and on the physical processes driving the transition from massive

[4] We assume $\alpha_{\rm B} = 2.6 \times 10^{-13}\,{\rm cm^3\,s^{-1}}$, which is valid for hydrogen at $T = 10^4$ K, e.g. Maselli et al. (2003).

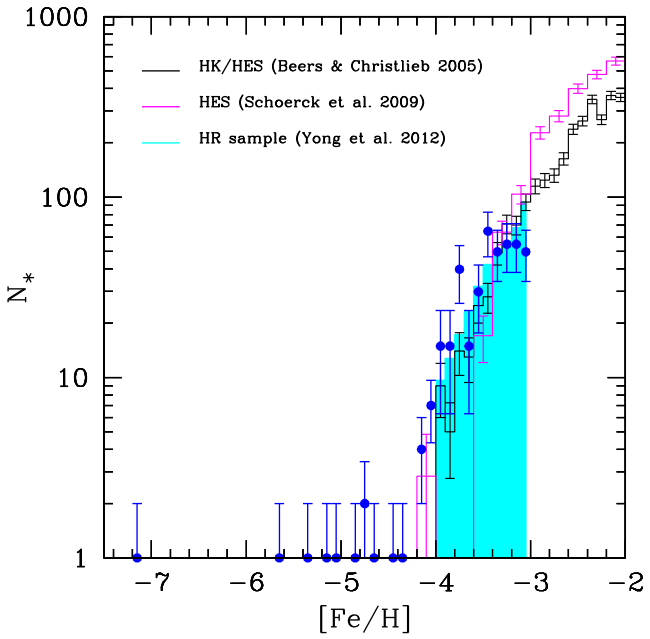


**Figure 5.** The Galactic halo MDFs obtained using different data sets and normalized to the same number of stars at [Fe/H] $\leq -3$. Histograms show the result from: black – the medium resolution HK and HES surveys (Beers & Christlieb 2005); magenta – the HES survey corrected for observational biases and incompleteness (Schörck et al. 2009); cyan shaded – the homogeneous sample of high-resolution (HR) spectroscopic data from Yong et al. (2013), corrected to account for incompleteness and observational errors. The blue points show the uncorrected sample by Yong et al. (2013) to which we added HR data for stars with [Fe/H] $< -4$, taken from recent literature (see text for details and references). Error bars represent Poissonian errors.

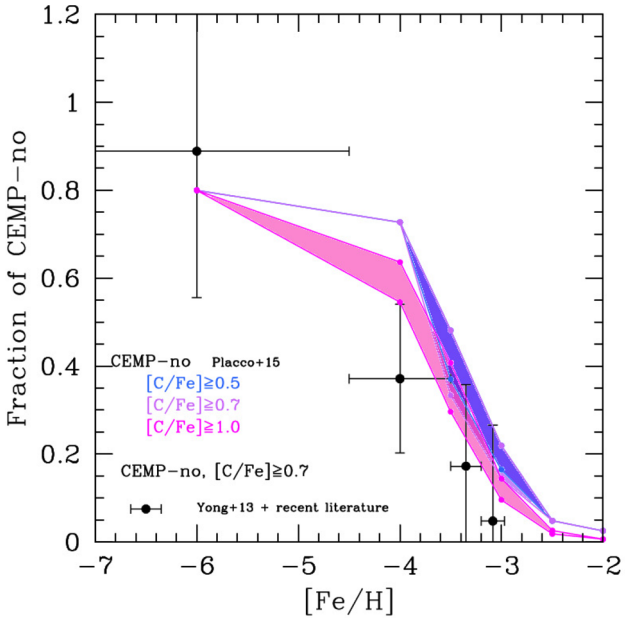


**Figure 6.** Fraction of CEMP-no stars versus [Fe/H] obtained using different data and [C/Fe] cuts for CEMP-no stars (see the labels). We show results from: high-resolution sample by Yong et al. (2013) that we completed by adding more recent literature data (points with Poissonian error bars); the larger high/medium-resolution sample by Placco et al. (2013) (connected coloured points) that the authors corrected to account for carbon depletion due to internal mixing processes (upper points). The shaded area quantifies such a correction.

Pop III stars to normal Pop II stars (Tumlinson 2006, 2010; Komiya et al. 2007; Salvadori et al. 2007, 2010; de Bennassuti et al. 2014; Hartwig et al. 2015; Komiya, Suda & Fujimoto 2016).

In Fig. 5, we show the most recent determinations of the low-Fe tail of the Galactic halo MDF as derived by various groups, which exploited different data sets. By normalizing the MDFs to the same cumulative number of stars at [Fe/H] $\leq -3$ we compare the results from: (i) the joint HK and HES medium-resolution surveys, which provide $\approx$2765 stars at [Fe/H] $< -2$ (Beers & Christlieb 2005); (ii) the HES survey, which collected $\approx$1500 stars at [Fe/H] $< -2$ (e.g. Christlieb et al. 2008); the derived MDF has been corrected by Schörck et al. (2009) to account for observational biases and incompleteness; (iii) the high-resolution sample by Yong et al. (2013), who collected a homogeneous ensemble of $\approx$95 stars at [Fe/H] $\leq -2.97$ by combining data from the literature along with program stars. Following Schörck et al. (2009), Yong and collaborators corrected the high-resolution MDF by using the HES completeness function. Furthermore, they accounted for the Gaussian error associated with each [Fe/H] measurements, and derived a realistically smoothed MDF (see their section 3.2 and Fig. 5). The effects of these corrections can be appreciated by comparing the final high-resolution (HR) MDF in Fig. 5 (shaded area), and the points with error bars within $-4 \leq$ [Fe/H] $\leq -3$, which represent the raw data.

By inspecting Fig. 5 we can see that the MDFs obtained with the high-resolution sample by Yong et al. (2013) and the joint HK and HES samples by Beers & Christlieb (2005) are in excellent agreement. Both MDFs continuously decrease between [Fe/H] $\approx -3$ and [Fe/H] $\approx -4$ spanning roughly one order of magnitude in $N_*$. On the other hand, the HES sample underestimates the total number of stars at [Fe/H] $\leq -3.7$. As discussed by Yong et al. (2013), this is likely due to the selection criteria exploited by the HES sample, which reject stars with strong *G* bands. As high-resolution observations provide more precise [Fe/H] measurements, we use the small HR sample by Yong and collaborators as our 'reference MDF' for $-4 <$ [Fe/H] $< -3$. At lower [Fe/H], we complete the sample by adding all the stars that have been discovered during the years and followed-up at high-resolution (see points in Fig. 5). Thus, the reference MDF we compare our models with rapidly declines with decreasing [Fe/H], exhibits a sharp cut-off at [Fe/H] $= -4.2 \pm 0.2$ and a low-Fe tail made by nine stars that extends down to [Fe/H] $\approx -7.2$ (Keller et al. 2014).

Interestingly, eight out of the nine Galactic halo stars identified at [Fe/H] $< -4.5$ show high overabundance of carbon, [C/Fe] $> 0.7$ (Christlieb et al. 2002; Frebel et al. 2005, 2015; Norris et al. 2007; Keller et al. 2014; Allende Prieto et al. 2015; Bonifacio et al. 2015; Hansen et al. 2015; Meléndez et al. 2016, see for example fig. 1 from Salvadori et al. 2015). Although only five of these CEMP stars have available measurements of slow- and rapid-neutron capture process elements (s-/r-), which have subsolar values, all of them can be likely classified as 'CEMP-no' stars (e.g. see discussion in Norris et al. 2010; Bonifacio et al. 2015). CEMP-no stars do not show s-process elements that are produced by AGB stars (e.g. Beers & Christlieb 2005), they are not preferentially associated with binary systems (e.g. Hansen, Andersen & Nordtröm 2013), and they most likely appear at low [Fe/H] (see Fig. 6). For these reasons, the chemical abundances measured in their photospheres are believed to reflect their environment of formation, which was likely polluted by Pop III stars that developed mixing and fallback evolving as 'faint SNe' (e.g. Bonifacio et al. 2003; Iwamoto et al. 2005; Marassi et al. 2014), or by primordial 'spinstars', which experienced mixing and mass

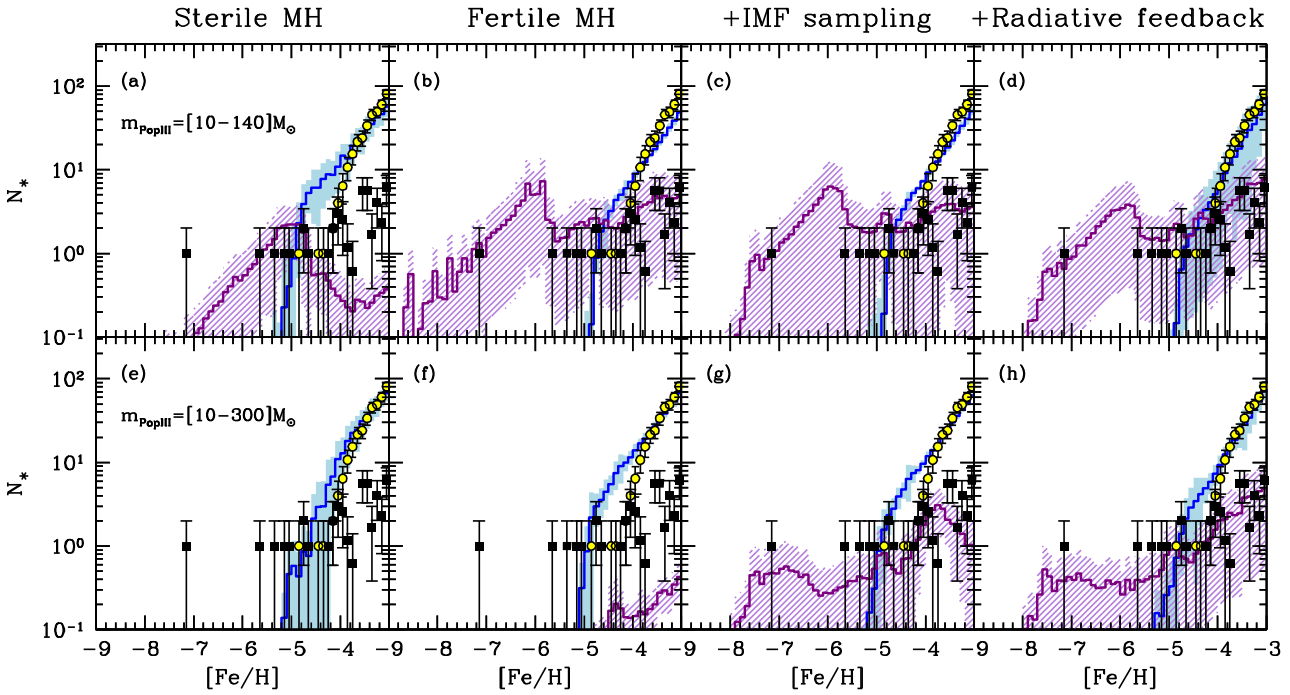


**Figure 7.** Comparison between observed (points with Poissonian error bars) and simulated (histograms with shaded areas) Galactic halo MDFs, where we differentiate the contribution of C-enhanced (purple histograms with striped-dashed shaded areas and black filled squares) and C-normal (blue histograms with filled shaded areas and yellow filled circles) stars. Pop III stars are assumed to form either in the range [10–140] $M_\odot$ (top panels) or [10–300] $M_\odot$ (bottom panels, see also labels). From left to right we show the results for models with: sterile minihaloes (panels a–e); fertile minihaloes with a temperature-regulated star formation efficiency (panels b–f); fertile minihaloes with a temperature-regulated star formation efficiency and a stochastically sampled Pop III IMF (panels c–g); fertile minihaloes with a star formation efficiency regulated by radiative feedback and a stochastically sampled Pop III IMF (panels d–h).

loss because of high rotational velocities (e.g. Meynet et al. 2006; Maeder et al. 2015).

In Fig. 6 we show the fraction of CEMP-no stars in different [Fe/H] bins, $F_{\rm CEMP-no} = N_{\rm CEMP-no}({\rm [Fe/H]})/N_*({\rm [Fe/H]})$, derived by using the HR sample by Yong et al. (2013) along with new literature data. Following Yong et al. (2013), we select the iron bins in order to have a roughly equal number of stars in each of them, $N_* \approx 30$. Only in the lowest bin, [Fe/H] $< -4.5$, the total number of stars is limited to $N_* = 9$. This is reflected in the larger Poissonian errors. In Fig. 6 we also show the $F_{\rm CEMP-no}$ values obtained by using the available data and CEMP-no classification by Placco et al. (2014). These authors exploited a larger sample of high- and medium-resolution observations. Furthermore, they corrected the carbon measurements in red giant branch (RGB) stars in order to account for the depletion of the surface carbon abundance, which is expected to occur during the RGB phase. We can see that in both samples $F_{\rm CEMP-no}$ rapidly decreases with increasing [Fe/H], and that the results are consistent within the Poissonian errors. However, as already noticed by Frebel & Norris (2015), the estimated CEMP-no fraction is higher in the sample by Placco et al. (2014). To be consistent with our reference MDF and limit our comparison to high-resolution data only, we will focus on the $F_{\rm CEMP-no}$ values derived by using Yong et al. (2013) and new literature data. However we should keep in mind that these are likely lower limits on the actual CEMP-no fraction at [Fe/H] $> -4.5$.

## 4 RESULTS

In this section we present the results of our models by focusing on the MDF and on the properties of CEMP-no stars at [Fe/H] $< -3$. Since we did not model mass transfer in binary systems, we will completely neglect CEMP-s/(rs) stars in our discussion (see also Salvadori et al. 2015).

The comparison between simulated and observed MDFs is shown in Fig. 7 where the two functions have been normalized to the same number of observed stars at [Fe/H] $< -3$ (see Section 3). We computed the mean theoretical MDF as the average number of stars in each [Fe/H] bin across the 50 merger histories. The $1\sigma$ dispersion, or standard deviation, is then derived as the square root of the variance among the 50 merger histories. Once these quantities are evaluated the normalization is done by rescaling the total number of simulated star at [Fe/H] $< -3$ to the observed value. Note that the same results are obtained by first normalizing the simulated MDF of each realization, and then computing the average MDF and $1\sigma$ dispersion.

By inspecting all the panels, from left to right, we can see how the different physical processes included in the models affect the shape of the MDF, along with the predicted number of CEMP-no stars. For each model, the figure shows how the results vary when we assume Pop III stars to form with masses in the range [10–140] $M_\odot$ (top panels), where only faint SNe can contribute to metal enrichment, and [10–300] $M_\odot$ (bottom panels), where both faint SNe and PISNe can produce and release heavy elements.

Panels (a) and (e) show the results for models with 'sterile' minihaloes, i.e. assuming that systems with $T_{\rm vir} < 10^4$ K are not able to form stars. As discussed in de Bennassuti et al. (2014), we see that both the low-Fe tail of the MDF, at [Fe/H] $< -5$, and the number of CEMP-no stars, can only be reproduced when the Pop III stars have masses $m_{\rm PopIII} = $ [10–140] $M_\odot$ (panel a). This is because CEMP-no stars form in environments enriched by the chemical products of primordial faint SNe, which produce large amount of C and very low Fe. These key chemical signatures are completely washed out

if PISNe pollute the same environments (panel e), because of the large amount of Fe and other heavy elements that these massive stars produce (≈50 per cent of their masses). Panel (a) also shows that, although the overall trend is well reproduced, the model predicts an excess of C-normal stars at [Fe/H] $< -4$, and it underestimates the observations at [Fe/H] $< -6$. In other words, the slope of the total MDF (blue+purple histograms) is predicted to be roughly constant, at odds with observations (see also Section 3 and the discussion in de Bennassuti et al. 2014).

The results change when minihaloes are assumed to be 'fertile' (panels b and f) and their star formation efficiency is assumed to be simply regulated by their virial temperature (see Section 2.1). Note that the evolution of the minimum halo mass for star formation assumed in this case (Salvadori & Ferrara 2009, 2012) is consistent with the mass threshold for efficient $H_2$ cooling obtained by adopting the LW background of Ahn et al. (2009), as it has been shown by Salvadori et al. (2014).

Panel (b) shows that the overall MDF has a different shape with respect to panel (a): it rapidly declines around [Fe/H] $\approx -4.5$ and shows a low-Fe tail that extends down to [Fe/H] $\approx -8$ and that is made by CEMP-no stars *only*. Such a discontinuous shape, which is consistent with observations, reflects the different environment of formation of CEMP-no and C-normal stars (see also the discussion in Salvadori, Skuladottir & de Bennassuti 2016). CEMP-no stars are formed in low-mass minihaloes at a very low and almost constant rate (e.g. Salvadori et al. 2015). C-normal stars, instead, predominantly form in more massive systems, which more efficiently convert gas into stars, producing the rapid rise of the MDF at [Fe/H] $> -5$.

The comparison between panels (b) and (c) shows that when $m_{\rm PopIII} = [10\text{–}140]\,{\rm M}_{\odot}$ the MDF does not depend on the incomplete sampling of the Pop III IMF (see Section 2.2). However, the picture changes when $m_{\rm PopIII} = [10\text{–}300]\,{\rm M}_{\odot}$ (panel g). Because of the poor sampling of the Pop III IMF in minihaloes, the formation of stars in the faint SN progenitor mass range is strongly favoured with respect to more massive PISN progenitors (Fig. 2). As a consequence, the chemical signature of primordial faint SNe is retained in most minihaloes, where CEMP-no stars at [Fe/H] $< -4$ preferentially form. Furthermore, because of the reduced number of Pop III haloes imprinted by primordial faint SN *only*, the amplitude of the low-Fe tail is lower than in panel (c), and thus in better agreement with observations.

Panels (d) and (h) show the results obtained by self-consistently computing the star formation efficiency in minihaloes (Section 2.1). We note that there are no major changes with respect to panels (c) and (g), meaning that our implementation of the radiative feedback described in Section 2.3 is consistent with the simple analytical prescriptions used in panels (c) and (g). In other words, our model results do not depend strongly on the LW flux (upper panel of Fig. 4), which in such a biased region of the Universe is expected to be larger than in the average cosmic volume (e.g. Ahn et al. 2009; Xu et al. 2016). Still, three important differences can be noticed by inspecting panels (d) and (h): (i) the number of C-normal stars shows a larger scatter than previously found, (ii) their excess with respect to the data is partially reduced, and (iii) the number of CEMP-no star with [Fe/H] $> -4$ is larger, and thus in better agreement with available data. These are consequences of the modulation of minihaloes star formation efficiency, which declines with cosmic time as a consequence of the decreasing mean gas density and of the increasing radiative feedback effects by the growing LW background (Fig. 1). This delays metal enrichment, preserving the C-rich signatures of faint SNe in the smallest Lyman $\alpha$ cooling haloes, where CEMP-no stars with [Fe/H] $> -4$ can form with higher efficiency.

We finally note that in all models the scatter of the MDF is much larger for the CEMP component than for the C-normal one. This is due to the broad dispersion among different merger histories at $z > 10$ (see fig. 4 of de Bennassuti et al. 2014), where the CEMP MDF is built (see their fig. 10).

When $m_{\rm PopIII} = [10\text{–}140]\,{\rm M}_{\odot}$, furthermore, a bump in the simulated CEMP MDF is observed. This is due to the fact that in this case Pop III stars evolve only as faint SNe, polluting the ISM of their hosting (mini)haloes around $[{\rm Fe/H}]_{\rm PopIII} \approx -6$, a value that is settled by the Fe yields of faint SNe and mean star formation efficiency of minihaloes (for more massive Ly$\alpha$ cooling haloes $[{\rm Fe/H}]_{\rm PopIII} \sim -5$). Once normal Pop II stars begin to evolve as core-collapse SNe, the Fe enrichment is much faster because of the larger Fe yields. Thus, the ISM is enriched up to higher [Fe/H], giving origin to the bump of CEMP stars.

When we assume $m_{\rm PopIII} = [10\text{–}300]\,{\rm M}_{\odot}$, we obtain a better agreement with the data at [Fe/H] $> -4$, i.e. where the statistics of observed stars is higher. However at lower metallicities, $-5 <$ [Fe/H] $< -4$, we can see that both models overpredict the total number of stars with respect to current data. But how significant is the number of observed stars at these [Fe/H]? In the top panel of Fig. 8 we plot the result of our fiducial model for $m_{\rm PopIII} = [10\text{–}300]\,{\rm M}_{\odot}$, also including the *total* MDF and the intrinsic errors induced by observations (grey shaded area). These errors are evaluated by using a Monte Carlo technique that randomly selects from the theoretical MDF a number of stars equal to the observed one (see section 5 of Salvadori et al. 2015). The results, which represent the average value $\pm 1\sigma$ errors among 1000 Monte Carlo samplings, allow us to quantify the errors induced by the limited statistics of the observed stellar sample. We can see that at [Fe/H] $< -4$ these errors are larger than the spread induced by different realizations, implying that the statistics should increase before drawing any definitive conclusions (see also Section 5 for a discussion). We can then have a look to other observables.

### 4.1 CEMP and carbon-normal stars

In the middle panel of Fig. 8 we compare our model results with the available measurements of the [C/Fe] ratio for Galactic halo stars at different [Fe/H]. Our findings show a decreasing [C/Fe] value for increasing [Fe/H], in good agreement with observations. According to our results, stars at [Fe/H] $< -5$ formed in minihaloes polluted by primordial faint SNe (see also Fig. 9). When these stars explode, they release large amounts of C and very small of Fe, i.e. $[{\rm C/Fe}]_{\rm ej} > 4$, thus *self-enriching* the ISM up to total metallicities $Z > 10^{-4}\,{\rm Z}_{\odot}$. The subsequent stellar generations formed in these minihaloes are thus 'normal' Pop II stars. Their associated core-collapse SNe further enrich the ISM with both Fe and C, i.e. $[{\rm C/Fe}]_{\rm ej} \approx 0$, thus producing a gradual decrease of [C/Fe] at increasing [Fe/H]. Such a trend is reflected in the chemical properties of long-lived CEMP-no stars that formed in these environments (see middle panel of Fig. 8).

When and where do the most metal-poor C-normal stars form? We find that at [Fe/H] $< -4.5$, C-normal stars can only form in haloes with a dust-to-gas ratio above the critical value, and that have *accreted their metals and dust from the surrounding MW environment*. When this occurs, normal Pop II SNe in self-enriched haloes have already become the major contributors to the metal enrichment of the external MW environment, leading to [C/Fe] $< 0.7$ (see also the middle panel of fig. 7 in de Bennassuti et al. 2014). As

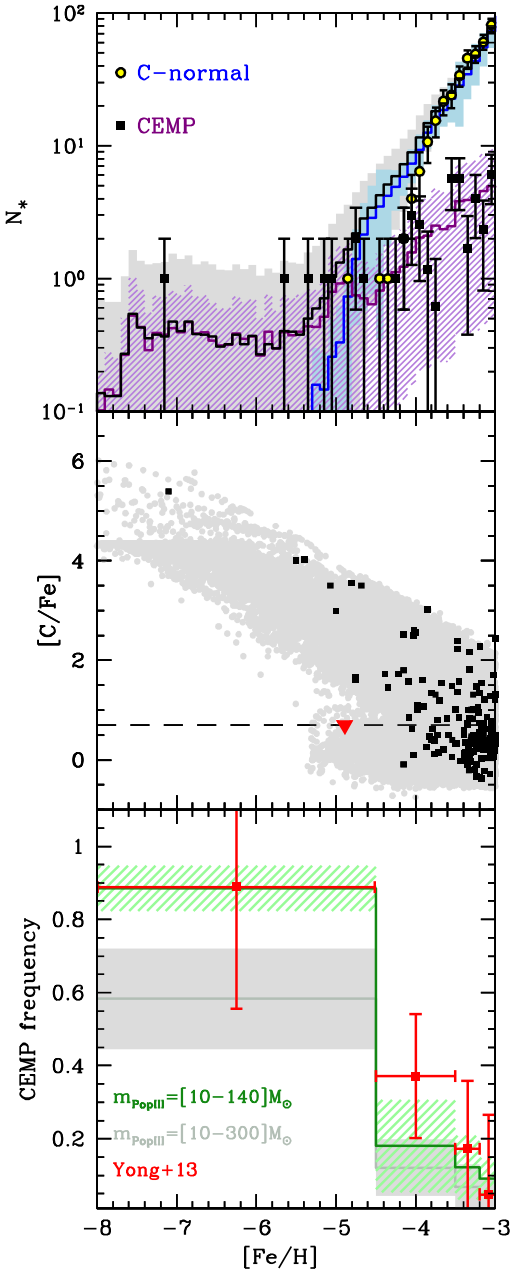


**Figure 8.** Top: same as panel (h) in Fig. 7, but with the inclusion of the total MDF and errors induced by the observations, which have been obtained using a Monte Carlo selection procedure (see text). Middle: stellar [C/Fe] versus [Fe/H] measured in Galactic halo stars (black squares, see fig. 1 of Salvadori et al. 2015) and obtained in 50 realizations of our fiducial model for $m_{\rm PopIII} = [10–300]\,{\rm M}_{\odot}$ (grey dots). The red triangle at [Fe/H] $\sim -5$ shows the upper limit for the only C-normal metal-poor star observed at [Fe/H] $\lesssim -4.5$ so far (Caffau et al. 2011). The line shows the value of [C/Fe] = 0.7, which discriminates between CEMP-no and C-normal stars. Bottom: comparison between the observed fraction of CEMP-no stars (points with Poissonian error bars as explained in Section 3) and the fraction predicted by our fiducial models for different Pop III mass ranges: $m_{\rm PopIII} = [10–140]\,{\rm M}_{\odot}$ as green histogram with striped-dashed shaded area; $m_{\rm PopIII} = [10–300]\,{\rm M}_{\odot}$ as grey histogram with filled shaded area.

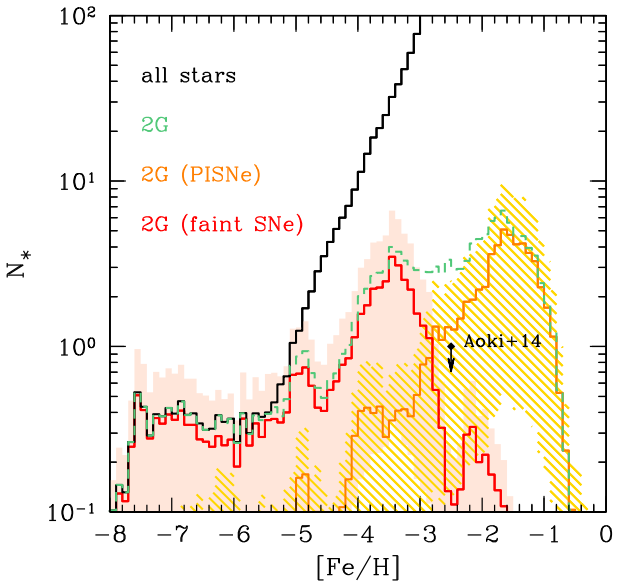


**Figure 9.** Simulated average MDF for all stars (black histogram) and for 2G stars (dashed green histogram), selecting them as stars formed in environments where metals come mostly (>50 per cent) from Pop III stars. The red (orange) histogram represents 2G stars with a dominant (>50 per cent) metal contribution from Pop III faint SNe (PISNe) and the filled (striped-dashed) region represents the $1\sigma$ dispersion. The upper limit at [Fe/H] $= -2.5$ represents the recent observation of a star with chemical imprint of PISNe (Aoki et al. 2014).

star formation proceeds in these Pop II haloes, more core-collapse SNe contribute to self-enrichment of these environments, thus further increasing [Fe/H] with an almost constant [C/Fe]. This creates the horizontal branch shown in the middle panel of Fig. 8 within [Fe/H] $\approx [-5, -3]$. In this region of the plot, we note that the model predicts a larger concentration of C-normal stars than currently observed.

In the bottom panel of Fig. 8 we compare the expected frequency of CEMP-no stars at different [Fe/H] with the available data (see Section 3). We can see that our models overestimate the contribution of C-normal stars at [Fe/H] $< -4$. Interestingly, a better agreement is obtained when the mass of Pop III stars is limited to the range $m_{\rm PopIII} = [10–140]\,{\rm M}_{\odot}$, since more faint SNe are produced. The number of stars observed at [Fe/H] $< -4$ is limited to $\approx$10 (see Section 3). Furthermore, such a discrepancy between model and data might also be connected to some underlying physical processes that cannot be captured by the model, as we will extensively discuss in Section 5. In conclusion, Pop III stars with masses $m_{\rm PopIII} = [10–300]\,{\rm M}_{\odot}$ are favoured by our analysis. Such a model better matches the overall shape of the MDF of CEMP-no and C-normal stars, and it is also in better agreement with data at [Fe/H] $> -4$ (compare panels d and h of Fig. 7). Only at these high [Fe/H] the intrinsic observational errors are lower than the dispersion induced by different merger histories (see top panel of Fig. 8), making the difference between model and data statistically significant.

### 4.2 Predictions for second-generation stars

Our analysis of the Galactic halo MDF and properties of CEMP-no versus C-normal stars supports the most recent findings of numerical simulations for the formation of the first stars, which indicate that Pop III stars likely had masses in the range $m_{\rm PopIII} = [10–300]\,{\rm M}_{\odot}$.

We make one step further, and we quantify the expected number and typical [Fe/H] values of second-generation (2G) stars, i.e. stars that formed in gaseous environments that were predominantly polluted by Pop III stars (Salvadori et al. 2007).

In Fig. 9 we show the predictions for our fiducial model with $m_{\rm PopIII} = [10–300]\,{\rm M}_\odot$. The figure illustrates the total distribution of 2G stars formed in environments in which Pop III stars provided $\geq$50 per cent of the total amount of metals (green). Furthermore, it shows the individual distributions for 2G stars imprinted by faint SNe (red) and PISNe (orange). It is clear that the total number of 2G stars represents an extremely small fraction of the Galactic halo population, in full agreement with previous studies (Salvadori et al. 2007; Karlsson, Johnson & Bromm 2008). Furthermore, we can see that the distributions of 2G stars polluted by faint SNe and PISNe are extremely different. Because of the low amount of Fe released by faint SNe, 2G stars enriched by this stellar population predominantly appear at [Fe/H] $< -3$. Interestingly, we find that their distribution essentially matches that of CEMP-no stars (see Fig. 8), representing $\approx$100 per cent of the observed stellar population at [Fe/H] $< -5$. In other words, *our model predicts that all CEMP-no stars in this [Fe/H] range have been partially imprinted by Pop III faint SNe*. On the contrary, we see that the distribution of 2G stars polluted by PISNe is shifted towards higher [Fe/H] values. This is because massive PISNe produce larger amount of iron than faint SNe, thus self-enriching their birth environments up to [Fe/H] $> -4$. In fact, for $m_{\rm PopIII} = [10–300]\,{\rm M}_\odot$, the Fe yielded by PISN per total stellar mass formed, $M_*$, is $Y_{\rm Fe}^{\rm PISN} \approx M_{\rm Fe}/M_* \approx 2.7 \times 10^{-2}$, which is several orders of magnitude larger than the one produced by faint SNe. As described in Section 2.2 a minihalo can likely host a PISN if it forms a stellar mass $M_* \gtrsim 10^4\,{\rm M}_\odot$ which implies a Fe production of $M_{\rm Fe} \gtrsim 270\,{\rm M}_\odot$. According to our prescription for star formation, the typical mass of such a minihalo is $\sim 10^8\,{\rm M}_\odot$, meaning that this amount of Fe can be dispersed in a gaseous environment of $\sim 10^7\,{\rm M}_\odot$, assuming the cosmological baryon fraction. This leads to an ISM polluted at [Fe/H] $\sim -1.8$, which is consistent with the peak of 2G stars with PISN imprint predicted by our model (see Fig. 9). Unfortunately, at these [Fe/H] the Galactic halo population is dominated by stars formed in environments mostly polluted by normal Pop II SNe (see Section 4.1). This makes the detection of 2G stars imprinted by PISNe very challenging.

In the upper (lower) panel of Fig. 10 we quantify the cumulative (differential) fraction of 2G stars imprinted by PISNe with respect to the overall stellar population as a function of [Fe/H]. In both panels we identify 2G stars that formed in environments where 50, 80, and 99 per cent of the metals were coming from PISNe. We can clearly see that 2G stars always represent <3 per cent of the total stellar population. Furthermore, the cumulative fraction of 2G stars polluted by PISN at 50 per cent (80 per cent) level, strongly decreases with increasing [Fe/H]: around [Fe/H] $= -2$, in particular, these 2G stars are predicted to represent 0.25 per cent (0.1 per cent) of the total stellar population, which is fully consistent with current observations (see point in Fig. 10). Indeed, among the $\approx$500 Galactic halo stars analysed so far at [Fe/H] $< -2$, there is only one candidate at [Fe/H] $\approx -2.4$ that might have been imprinted by a PISN (Aoki et al. 2014). This rare Galactic halo star shows several peculiar chemical elements in its photosphere, which might reflect an ISM of formation enriched by both massive PISNe and normal core-collapse SNe (Aoki et al. 2014). In Fig. 10 we can see that 2G stars imprinted by the chemical products of PISNe *only*, represent <0.1 per cent of the total Galactic halo population (top), and they are predicted to be more frequent at $-3 <$ [Fe/H] $< -2$ (bottom).

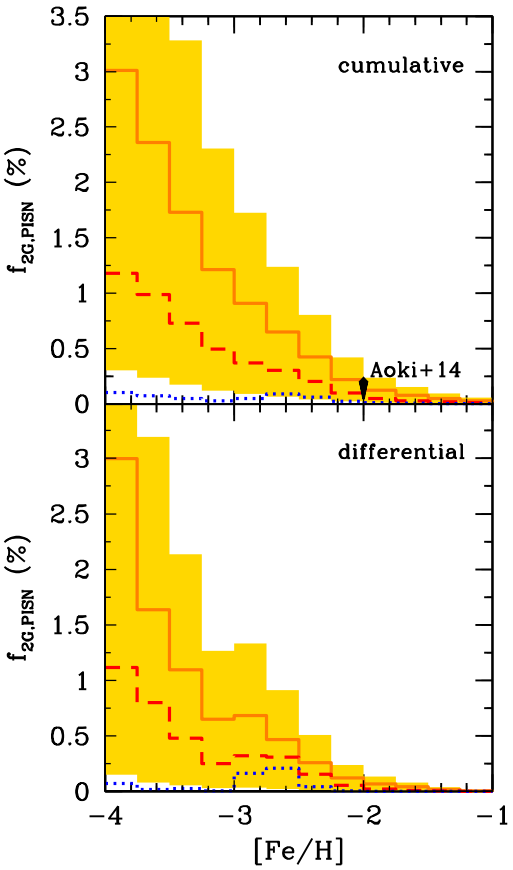


**Figure 10.** Cumulative (top) and differential (bottom) fraction (per cent) of 2G stars imprinted by PISNe with respect to the total number of stars in different [Fe/H] bins. The colours show the percentage of 2G stars formed in environments where metals from PISNe correspond to at least 50 per cent (solid orange), 80 per cent (dashed red), and 99 per cent (dotted blue) of the total. The yellow shaded area is the $1\sigma$ dispersion for the 50 per cent case. The data point is from Aoki et al. (2014), who possibly detected the chemical imprint of PISNe (upper limit) in one out of 500 stars at [Fe/H] $< -2$.

### 4.3 Varying the Pop III IMF

We can finally analyse the dependence of our findings on the slope and mass range of the Pop III IMF. These results are shown in Fig. 11, where we compare our reference model (left), with two alternative choices of the Pop III IMF, inspired by numerical simulations: a flat IMF with $m_{\rm PopIII} = [10–300]\,{\rm M}_\odot$ (e.g. Hirano et al. 2014), and a Larson IMF with $m_{\rm PopIII} = [0.1–300]\,{\rm M}_\odot$ and a characteristic mass $m_{\rm ch} = 0.35\,{\rm M}_\odot$ (e.g. Stacy et al. 2016).

The low-Fe tail of the MDF, and thus the number and distribution of CEMP-no stars, strongly depends on the Pop III IMF. When a flat IMF is considered (middle panel of Fig. 11), less CEMP-no stars are produced with respect to the reference case (left-hand panel), both at low and at high [Fe/H]. This is due to the smaller fraction of faint SNe with respect to the total mass of Pop III stars formed. This is equal to $\approx$1.5 per cent for a flat IMF, and $\approx$70 per cent for a Larson IMF, where these numbers have been obtained by integrating the normalized IMFs in the mass range [8–40] ${\rm M}_\odot$. Such a large difference is partially mitigated by the incomplete sampling of the Pop III IMF in inefficient star-forming minihaloes (see Section 2.2). Still, the different IMF slope decreases substantially the number of CEMP-no stars, making the flat IMF model *partially inconsistent* with current data sets.

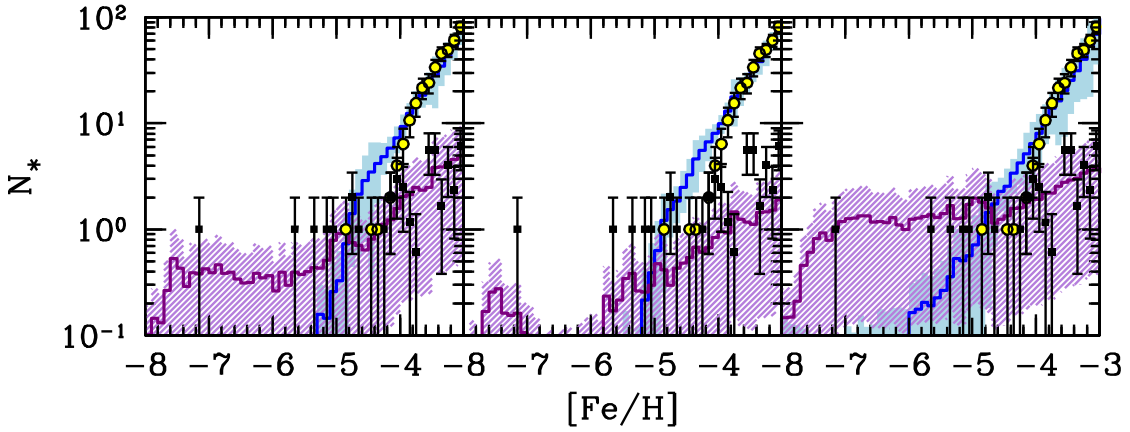


**Figure 11.** Comparison between the observed and simulated Galactic halo MDFs (see Fig. 7) obtained by using different IMF for Pop III stars: a Larson IMF with $m_{\rm PopIII} = [10–300]\,{\rm M}_\odot$ and $m_{\rm ch} = 20\,{\rm M}_\odot$ (left), a flat IMF with $m_{\rm PopIII} = [10–300)]\,{\rm M}_\odot$ (middle), and a Larson IMF with $m_{\rm PopIII} = [0.1–300]\,{\rm M}_\odot$ and $m_{\rm ch} = 0.35\,{\rm M}_\odot$ (right).

On the other hand, when the Pop III IMF is extended down to lower masses, $m_{\rm PopIII} = [0.1–300]\,{\rm M}_\odot$, the number of CEMP stars increases with respect to the reference model (right versus left-hand panels of Fig. 11). However, if we make the same calculation as before, we find faint SNe to represent ≈1 per cent of the total Pop III stellar mass, substantially less than in our reference model. The larger number of CEMP stars at low [Fe/H] must then have a different origin.

At [Fe/H] <−5, we predict that ≈35 per cent[5] of 2G CEMP stars (≈15 per cent of the total number of stars) have been imprinted by a mixed population of Pop III stars, including asymptotic giant branch (AGB) stars with $m_{\rm PopIII} = [2–10]\,{\rm M}_\odot$. In particular we find that these Pop III AGB stars might provide from ≈10 to ≈30 per cent of the total amount of heavy elements polluting the birth environment of these 2G stars. These CEMP stars, therefore, might also retain the peculiar chemical signature of Pop III AGB stars, such as the slow-neutron capture elements (e.g. Goriely & Siess 2001, 2004). In other words ≈35 per cent of these [Fe/H] < −5 stars might be CEMP-s stars rather than CEMP-no stars. This seems to be in contrast with current observational findings (e.g. Norris et al. 2010; Bonifacio et al. 2015) although more work needs to be done to rule out this Pop III IMF model. On the one hand detailed theoretical calculations are required to understand if Pop III AGB stars produce s-process elements at observable levels. On the other hand, a larger stellar sample at [Fe/H] <−5 is mandatory to robustly constrain the low-mass end of the Pop III IMF.

Furthermore the model predicts the existence of metal-free stars, as long as stars with $Z < 10^{-5}\,{\rm Z}_\odot$, that should respectively correspond to ≈0.15 and ≈0.3 per cent of the total number of stars at [Fe/H] < −3. As already discussed and quantified by several authors (Tumlinson 2006; Salvadori et al. 2007; Hartwig et al. 2015), this result might be in contrast with the current *non-detection* of metal-free stars. Yet, given the total number of stars collected at [Fe/H] < −3, which is ≈200, the fraction of zero-metallicity stars should be <1/200 = 0.5 per cent, which is still consistent with our findings.

[5] This is an average value for −8 < [Fe/H] < −5. Within this [Fe/H] range the percentages can vary from ≈20 to ≈60 per cent.

## 5 SUMMARY AND DISCUSSION

In this paper, we investigate the role that Pop III star-forming minihaloes play in shaping the properties of the MDF of Galactic halo stars and the relative fraction of CEMP-no and C-normal stars observed at [Fe/H] < −3. To this end, we use the merger tree code GAMETE (Salvadori et al. 2007, 2008), which we further implement with respect to recent studies for Galactic halo stars (de Bennassuti et al. 2014) to resolve $H_2$-cooling minihaloes with $T_{\rm vir} < 10^4$ K, which are predicted to host the first, Pop III stars (e.g. Abel et al. 2002; Hirano et al. 2014). Following de Bennassuti et al. (2014), we initially assumed Pop III stars to have masses in the range [10–300] $\,{\rm M}_\odot$, and to be distributed according to a Larson IMF (Fig. 2). We subsequently explored the dependence of our results on different IMF slope and Pop III mass range. In all cases, we assumed that Pop III stars with masses $m_{\rm PopIII} = [10–40]\,{\rm M}_\odot$ evolved as faint SNe that experience mixing and fallback (e.g. Bonifacio et al. 2003; Umeda & Nomoto 2003; Iwamoto et al. 2005; Marassi et al. 2014, 2015).

To accurately model the formation of Pop III stars, we introduce a new random IMF selection procedure, which allows us to account for the incomplete sampling of the Pop III IMF in inefficiently star-forming minihaloes. To compute the star formation efficiency of these low-mass systems, we exploit the results of numerical simulations by Valiante et al. (2016), who evaluate the cooling properties of $H_2$-cooling minihaloes as a function of (i) virial temperature, (ii) formation redshift, (iii) metallicity, and (iv) LW background. To this end, we self-consistently compute the LW and ionizing photon fluxes produced by MW progenitors, along with the reionization history of the MW environment, which is consistent with recent theoretical findings (Salvadori et al. 2014) and new observational data (Planck Collaboration XIII 2016; Planck Collaboration XLVII 2016).

The main results of our work, and their implications for theoretical and observational studies, can be summarized as follows.

(i) The shape of the low-Fe tail of the Galactic halo MDF is correctly reproduced only by accounting for star formation in minihaloes, which confirms their key role in the early phases of galaxy formation.

(ii) We demonstrate that it is fundamental to account for the poor sampling of the Pop III IMF in minihaloes, where inefficient Pop

III starbursts, with $<10^{-3}\,M_{\odot}\,yr^{-1}$, naturally limit the formation of $>100\,M_{\odot}$ stars and hence change the 'effective' Pop III IMF.

(iii) CEMP-no stars observed at [Fe/H] $< -3$ are found to be imprinted by the chemical products of primordial faint SNe, which provide >50 per cent of the heavy elements polluting their birth environment, making them 'second-generation' stars.

(iv) 2G stars imprinted by PISNe, instead, emerge at $-4 <$[Fe/H] $< -1$, where they only represent a few per cent of the total halo population, which makes their detection very challenging.

(v) At [Fe/H] $\approx -2$, only 0.25 per cent (0.1 per cent) of Galactic halo stars are expected to be imprinted by PISNe at >50 per cent (>80 per cent) level, in good agreement with current observations.

(vi) The low-Fe tail of the Galactic halo MDF and the properties of CEMP-no stars strongly depend on the IMF shape and mass range of Pop III stars.

A direct implication of our study is that the Galactic halo MDF is a key observational tool not only to constrain metal-enrichment models of MW-like galaxies and the properties of the first stars (Tumlinson 2006; Salvadori et al. 2007), but also the star formation efficiency of minihaloes. These observations, therefore, can be used to complement data-constrained studies of ultra-faint dwarf galaxies aimed at understanding the properties of the first star-forming systems (e.g. Bovill & Ricotti 2009; Salvadori & Ferrara 2009; Bland-Hawthorn, Sutherland & Webster 2015; Salvadori et al. 2015).

A key prediction of our model concerns the properties and frequency of 2G stars formed in gaseous environments imprinted by >50 per cent of heavy elements from PISNe. In agreement with previous studies (Salvadori et al. 2007; Karlsson et al. 2008), we find that these 2G stars are extremely rare, and we show that their MDF peaks around [Fe/H] $= -1.5$ (Fig. 9). In particular, 2G stars imprinted by PISNe *only* (>99 per cent level) are predicted to be more frequent at $-3 <$ [Fe/H] $< -2$, where they represent ≈0.1 per cent of the total. In the same [Fe/H] range, 2G stars polluted by PISNe at >50 per cent (>80 per cent) level, constitute ≈0.4 per cent (≈0.2 per cent) of the stellar population. These numbers are consistent with the unique detection of a rare halo star at [Fe/H] $\approx -2.5$ that has been possibly imprinted *also* by the chemical products of PISNe (Aoki et al. 2014).

On the other hand, we show that *C-enhanced stars at [Fe/H] $<-5$ are all truly 2G stars*. Hence, the number and properties of these CEMP stars can provide key indications on the Pop III IMF.

Given the current statistics, we show that a flat Pop III IMF with $m_{\rm PopIII} = [10\text{–}300]\,M_{\odot}$ is disfavoured by the observations. Furthermore, by assuming a Larson IMF with $m_{\rm PopIII} = [0.1\text{–}300]\,M_{\odot}$ and $m_{\rm ch} = 0.35\,M_{\odot}$, we find that on average ≈35 per cent of 2G CEMP stars at [Fe/H] $< -5$ are imprinted *also* by the chemical products of zero metallicity AGB stars. Such Pop III AGB stars can provide up to 30 per cent of the metals polluting the ISM of formation of these CEMP stars, which therefore might show the typical enhancement in s-process elements. This provides a prediction for the existence of Pop III stars with $m_{\rm PopIII} < 10\,M_{\odot}$, that can be tested by increasing the statistics of CEMP stars with available s-process measurements at [Fe/H] $< -5$ (e.g. Bonifacio et al. 2015).

As a final point, we recall that, with our fiducial model, we find a larger number of C-normal stars with $-5 <$ [Fe/H] $< -4$ than observed. As a consequence, in this [Fe/H] range the fraction of CEMP-to-C-normal stars is also lower than observed, although consistent with the data at $1\sigma$ level (Fig. 8). Several solutions for this small discrepancy do exist.

(i) The global contribution of Pop III stars to metal enrichment might have been underestimated in the model, which do not account for the *inhomogeneous mixing of metals* into the MW environment. Including this physical effect would naturally delay the disappearance of Pop III stars (Salvadori et al. 2014).

(ii) A fraction of Pop II stars with $m_{\rm PopII} = [10\text{–}40]\,M_{\odot}$ may evolve as faint SNe rather than normal core-collapse SNe, thus further contributing to enrich the gaseous environments with C, and reducing the formation of C-normal stars (de Bennassuti et al. 2014).

(iii) Another solution concerns *chemical feedback*. If we exclude the Caffau's star, the low-Fe tail of C-normal stars is consistent with $Z_{\rm cr} \approx 10^{-4.5}\,Z_{\odot}$, which means that these low-mass relics form *thanks to dust* but in environments that might correspond to higher $\mathcal{D}_{\rm cr}$ (or lower $f_{\rm dep}$) than we assumed here, where $Z_{\rm cr} = \mathcal{D}_{\rm cr}/f_{\rm dep}$ and $\mathcal{D}_{\rm cr}$ can be expressed as (Schneider et al. 2012b)

$$\mathcal{D}_{\rm cr} = [2.6\text{–}6.3] \times 10^{-9} \left[\frac{T}{10^3\,{\rm K}}\right]^{-1/2} \left[\frac{n_{\rm H}}{10^{12}\,{\rm cm}^{-3}}\right]^{-1/2}. \quad (10)$$

Here we have assumed the total grain cross-section per unit mass of dust to vary in the range $2.22 \leq S/10^5\,{\rm cm}^2/{\rm gr} \leq 5.37$, and a gas density and temperature where dust cooling starts to be effective equal to $n_{\rm H} = 10^{12}\,{\rm cm}^{-3}$ and $T = 10^3$ K. Since $S$ could vary in a broader interval depending on the properties of the SN progenitor, this might lead to a larger variation of the value of $\mathcal{D}_{\rm cr}$.

(iv) Since C-normal stars at $-5 \leq$ [Fe/H] $\leq -4$ predominantly form in MW progenitors which have $\mathcal{D} \geq \mathcal{D}_{\rm cr}$ and have accreted their heavy elements from the MW environment (as opposed to haloes that have been self-enriched by previous stellar generations), we might have overestimated the $\mathcal{D}$ of *accreted material*. In fact, no destruction is assumed to take place in SN-driven outflows, when the grains are mixed in the external medium, or during the phase of accretion on to newly formed haloes. Indeed, the null detection of C-normal stars with [Fe/H] $< -4.5$, beside the Caffau's star and despite extensive searches, might be an indication that, at any given $Z$, haloes accreting their heavy elements from the MW environment might be less dusty than self-enriched haloes.

(v) A final possibility pertains the effect of *inhomogeneous radiative feedback*, which might reduce (enhance) the formation of C-normal (C-enhanced) stars in minihaloes locally exposed to a strong (low) LW/ionizing radiation. These effects are expected to be particularly important at high-$z$, i.e. before the formation of a global uniform background (Graziani et al. 2015).

Although all these solutions are plausible, we should not forget that our comparison is actually based on 10 stars at [Fe/H] $< -4$, which makes the intrinsic observational errors larger than those induced by different merger histories of the MW (Fig. 8, upper panel). This underlines the quest for more data to better understand the intricate network of physical processes driving early galaxy formation.

## ACKNOWLEDGEMENTS

We acknowledge D. Yong for kindly sharing his data, P. Bonifacio, T. Beers, N. Christlieb, and P. Molaro for useful discussions, and the anonymous referee for a constructive and useful report. We thank the Kapteyn Institute of Groningen for hosting MdB during the development of this project and the Kavli Institute for Theoretical Physics for hosting KO, SS, and RS during the completion of the work. The research leading to these results has received funding from the European Research Council under the European Union's

Seventh Framework Programme (FP/2007-2013)/ERC Grant Agreement no. 306476, from the National Science Foundation under Grant No. NSF PHY11-25915, and from the JSPS KAKENHI Grant No. 25287040. SS was partially supported by the Netherlands Organization for Scientific Research (NWO) through a VENI grant 639.041.233, and by the European Commission through a Marie Sklodowska–Curie Fellowship, project PRIMORDIAL 700907.

## REFERENCES

Abel T., Bryan G. L., Norman M. L., 2002, Science, 295, 93
Ahn K., Shapiro P. R., Iliev I. T., Mellema G., Pen U.-L., 2009, ApJ, 695, 1430
Allende Prieto C. et al., 2015, A&A, 579, A98
Aoki W., Tominaga N., Beers T. C., Honda S., Lee Y. S., 2014, Science, 345, 912
Barkana R., Loeb A., 2001, Phys. Rep., 349, 125
Beers T. C., Christlieb N., 2005, ARA&A, 43, 531
Beers T. C., Preston G. W., Shectman S. A., 1985, AJ, 90, 2089
Bessell M. S., Norris J., 1984, ApJ, 285, 622
Bianchi S., Schneider R., 2007, MNRAS, 378, 973
Bland-Hawthorn J., Sutherland R., Webster D., 2015, ApJ, 807, 154
Bocchio M., Marassi S., Schneider R., Bianchi S., Limongi M., Chieffi A., 2016, A&A, 587, A157
Bond J. R., Cole S., Efstathiou G., Kaiser N., 1991, ApJ, 379, 440
Bonifacio P., Molaro P., Beers T. C., Vladilo G., 1998, A&A, 332, 672
Bonifacio P., Limongi M., Chieffi A., 2003, Nature, 422, 834
Bonifacio P. et al., 2015, A&A, 579, A28
Bovill M. S., Ricotti M., 2009, ApJ, 693, 1859
Bromm V., 2013, Rep. Progress Phys., 76, 112901
Bruzual G., Charlot S., 2003, MNRAS, 344, 1000
Caffau E. et al., 2011, Nature, 477, 67
Christlieb N. et al., 2002, Nature, 419, 904
Christlieb N., Schörck T., Frebel A., Beers T. C., Wisotzki L., Reimers D., 2008, A&A, 484, 721
Crosby B. D., O'Shea B. W., Smith B. D., Turk M. J., Hahn O., 2013, ApJ, 773, 108
de Bennassuti M., Schneider R., Valiante R., Salvadori S., 2014, MNRAS, 445, 3039
Ferrara A., Salvadori S., Yue B., Schleicher D., 2014, MNRAS, 443, 2410
Frebel A. et al., 2005, Nature, 434, 871
Frebel A., Chiti A., Ji A. P., Jacobson H. R., Placco V. M., 2015, ApJ, 810, L27
Frebel A., Norris J. E., 2015, ARA&A, 53, 631
Gnedin N. Y., 2000, ApJ, 542, 535
Goriely S., Siess L., 2001, A&A, 378, L25
Goriely S., Siess L., 2004, A&A, 421, L25
Graziani L., Salvadori S., Schneider R., Kawata D., de Bennassuti M., Maselli A., 2015, MNRAS, 449, 3137
Greif T. H., 2015, Comput. Astrophys. Cosmol., 2, 3
Haardt F., Madau P., 1996, ApJ, 461, 20
Haiman Z., Rees M. J., Loeb A., 1997, ApJ, 476, 458
Hansen T., Andersen J., Nordtröm B., 2013, preprint (arXiv:1301.7208)
Hansen T. et al., 2015, ApJ, 807, 173
Hartwig T., Bromm V., Klessen R. S., Glover S. C. O., 2015, MNRAS, 447, 3892
Heger A., Woosley S. E., 2002, ApJ, 567, 532
Hirano S., Hosokawa T., Yoshida N., Umeda H., Omukai K., Chiaki G., Yorke H. W., 2014, ApJ, 781, 60
Hirano S., Hosokawa T., Yoshida N., Omukai K., Yorke H. W., 2015, MNRAS, 448, 568
Hosokawa T., Hirano S., Kuiper R., Yorke H. W., Omukai K., Yoshida N., 2016, ApJ, 824, 119
Iliev I. T., Scannapieco E., Shapiro P. R., 2005, ApJ, 624, 491
Ishigaki M. N., Tominaga N., Kobayashi C., Nomoto K., 2014, ApJ, 792, L32
Iwamoto N., Umeda H., Tominaga N., Nomoto K., Maeda K., 2005, Science, 309, 451
Kafle P. R., Sharma S., Lewis G. F., Bland-Hawthorn J., 2012, ApJ, 761, 98
Kafle P. R., Sharma S., Lewis G. F., Bland-Hawthorn J., 2014, ApJ, 794, 59
Karlsson T., Johnson J. L., Bromm V., 2008, ApJ, 679, 6
Keller S. C. et al., 2014, Nature, 506, 463
Komiya Y., Suda T., Minaguchi H., Shigeyama T., Aoki W., Fujimoto M. Y., 2007, ApJ, 658, 367
Komiya Y., Suda T., Fujimoto M. Y., 2016, ApJ, 820, 59
Machacek M. E., Bryan G. L., Abel T., 2001, ApJ, 548, 509
McMillan P. J., 2011, MNRAS, 414, 2446
Madau P., Ferrara A., Rees M. J., 2001, ApJ, 555, 92
Maeder A., Meynet G., Chiappini C., 2015, A&A, 576, A56
Marassi S., Chiaki G., Schneider R., Limongi M., Omukai K., Nozawa T., Chieffi A., Yoshida N., 2014, ApJ, 794, 100
Marassi S., Schneider R., Limongi M., Chieffi A., Bocchio M., Bianchi S., 2015, MNRAS, 454, 4250
Maselli A., Ferrara A., Ciardi B., 2003, MNRAS, 345, 379
Meléndez J., Placco V. M., Tucci-Maia M., Ramírez I., Li T. S., Perez G., 2016, A&A, 585, L5
Meynet G., Ekström S., Maeder A., 2006, A&A, 447, 623
Molaro P., Bonifacio P., 1990, A&A, 236, L5
Molaro P., Castelli F., 1990, A&A, 228, 426
Muñoz J. A., Madau P., Loeb A., Diemand J., 2009, MNRAS, 400, 1593
Noh Y., McQuinn M., 2014, MNRAS, 444, 503
Norris J. E., Ryan S. G., Beers T. C., 1997, ApJ, 489, L169
Norris J. E., Christlieb N., Korn A. J., Eriksson K., Bessell M. S., Beers T. C., Wisotzki L., Reimers D., 2007, ApJ, 670, 774
Norris J. E., Gilmore G., Wyse R. F. G., Yong D., Frebel A., 2010, ApJ, 722, L104
Okamoto T., Gao L., Theuns T., 2008, MNRAS, 390, 920
Oñorbe J., Boylan-Kolchin M., Bullock J. S., Hopkins P. F., Kereš D., Faucher-Giguère C.-A., Quataert E., Murray N., 2015, MNRAS, 454, 2092
Omukai K., 2012, PASJ, 64, 114
Omukai K., Nishi R., 1999, ApJ, 518, 64
O'Shea B. W., Wise J. H., Xu H., Norman M. L., 2015, ApJ, 807, L12
Parkinson H., Cole S., Helly J., 2008, MNRAS, 383, 557
Placco V. M., Frebel A., Beers T. C., Karakas A. I., Kennedy C. R., Rossi S., Christlieb N., Stancliffe R. J., 2013, ApJ, 770, 104
Placco V. M., Frebel A., Beers T. C., Stancliffe R. J., 2014, ApJ, 797, 21
Planck Collaboration XVI, 2014, A&A, 571, A16
Planck Collaboration XIII, 2016, A&A, 594, A13
Planck Collaboration XLVII 2016, A&A, preprint (arXiv:1605.03507)
Primas F., Molaro P., Castelli F., 1994, A&A, 290, 885
Raiteri C. M., Villata M., Navarro J. F., 1996, A&A, 315, 105
Ricotti M., Gnedin N. Y., Shull J. M., 2001, ApJ, 560, 580
Ryan S. G., Norris J. E., 1991, AJ, 101, 1835
Salvadori S., 2009, PhD thesis at SISSA/ISAS
Salvadori S., Ferrara A., 2009, MNRAS, 395, L6
Salvadori S., Ferrara A., 2012, MNRAS, 421, L29
Salvadori S., Schneider R., Ferrara A., 2007, MNRAS, 381, 647
Salvadori S., Ferrara A., Schneider R., 2008, MNRAS, 386, 348
Salvadori S., Dayal P., Ferrara A., 2010, MNRAS, 407, L1
Salvadori S., Tolstoy E., Ferrara A., Zaroubi S., 2014, MNRAS, 437, L26
Salvadori S., Skúladóttir Á., Tolstoy E., 2015, MNRAS, 454, 1320
Salvadori S., Skuladottir A., de Bennassuti M., 2016, Astron. Nachr., 337, 935
Schaerer D., 2002, A&A, 382, 28
Schneider R., Ferrara A., Natarajan P., Omukai K., 2002, ApJ, 571, 30
Schneider R., Ferrara A., Salvaterra R., 2004, MNRAS, 351, 1379
Schneider R., Omukai K., Inoue A. K., Ferrara A., 2006, MNRAS, 369, 1437
Schneider R., Omukai K., Bianchi S., Valiante R., 2012a, MNRAS, 419, 1566
Schneider R., Omukai K., Limongi M., Ferrara A., Salvaterra R., Chieffi A., Bianchi S., 2012b, MNRAS, 423, L60
Schörck T. et al., 2009, A&A, 507, 817

Simon J. D., Geha M., 2007, ApJ, 670, 313
Simon J. D., Frebel A., McWilliam A., Kirby E. N., Thompson I. B., 2010, ApJ, 716, 446
Skúladóttir Á., Tolstoy E., Salvadori S., Hill V., Pettini M., Shetrone M. D., Starkenburg E., 2015, A&A, 574, A129
Springel V. et al., 2005, Nature, 435, 629
Stacy A., Bromm V., Lee A. T., 2016, MNRAS, 462, 1307
Sternberg A., Le Petit F., Roueff E., Le Bourlot J., 2014, ApJ, 790, 10
Susa H., Hasegawa K., Tominaga N., 2014, ApJ, 792, 32
Takahashi K., Yoshida T., Umeda H., Sumiyoshi K., Yamada S., 2016, MNRAS, 456, 1320
Tominaga N., Umeda H., Nomoto K., 2007, ApJ, 660, 516
Tumlinson J., 2006, ApJ, 641, 1
Tumlinson J., 2010, ApJ, 708, 1398
Umeda H., Nomoto K., 2003, Nature, 422, 871
Valiante R., Schneider R., Salvadori S., Bianchi S., 2011, MNRAS, 416, 1916
Valiante R., Schneider R., Volonteri M., Omukai K., 2016, MNRAS, 457, 3356
van den Hoek L. B., Groenewegen M. A. T., 1997, A&AS, 123, 305
Wang W., Han J., Cooper A. P., Cole S., Frenk C., Lowing B., 2015, MNRAS, 453, 377
Wise J. H., Demchenko V. G., Halicek M. T., Norman M. L., Turk M. J., Abel T., Smith B. D., 2014, MNRAS, 442, 2560
Woosley S. E., Weaver T. A., 1995, ApJS, 101, 181
Xu H., Wise J. H., Norman M. L., Ahn K., O'Shea B. W., 2016, preprint (arXiv:1604.07842)
Yong D. et al., 2013, ApJ, 762, 27

This paper has been typeset from a TEX/LATEX file prepared by the author.